

# Hot Electron Diagnostic in a Solid Laser Target by Buried K-Shell Fluoror Technique from Ultra-Intense ( $3 \times 10^{20} \text{ W/cm}^2$ , $\leq 500 \text{ J}$ ) Laser-Plasma Interactions on the Petawatt Laser at LLNL

*K. Yasuike, M.H. Key, S.P. Hatchett, R.A. Snavely*

**U.S. Department of Energy**

Lawrence  
Livermore  
National  
Laboratory

**June 29, 2000**

## DISCLAIMER

This document was prepared as an account of work sponsored by an agency of the United States Government. Neither the United States Government nor the University of California nor any of their employees, makes any warranty, express or implied, or assumes any legal liability or responsibility for the accuracy, completeness, or usefulness of any information, apparatus, product, or process disclosed, or represents that its use would not infringe privately owned rights. Reference herein to any specific commercial product, process, or service by trade name, trademark, manufacturer, or otherwise, does not necessarily constitute or imply its endorsement, recommendation, or favoring by the United States Government or the University of California. The views and opinions of authors expressed herein do not necessarily state or reflect those of the United States Government or the University of California, and shall not be used for advertising or product endorsement purposes.

This work was performed under the auspices of the U. S. Department of Energy by the University of California, Lawrence Livermore National Laboratory under Contract No. W-7405-Eng-48.

This report has been reproduced directly from the best available copy.

Available electronically at <http://www.doe.gov/bridge>

Available for a processing fee to U.S. Department of Energy  
and its contractors in paper from  
U.S. Department of Energy  
Office of Scientific and Technical Information  
P.O. Box 62  
Oak Ridge, TN 37831-0062  
Telephone: (865) 576-8401  
Facsimile: (865) 576-5728  
E-mail: [reports@adonis.osti.gov](mailto:reports@adonis.osti.gov)

Available for the sale to the public from  
U.S. Department of Commerce  
National Technical Information Service  
5285 Port Royal Road  
Springfield, VA 22161  
Telephone: (800) 553-6847  
Facsimile: (703) 605-6900  
E-mail: [orders@ntis.fedworld.gov](mailto:orders@ntis.fedworld.gov)  
Online ordering: <http://www.ntis.gov/ordering.htm>

OR

Lawrence Livermore National Laboratory  
Technical Information Department's Digital Library  
<http://www.llnl.gov/tid/Library.html>

**Hot electron diagnostic in a solid laser target by buried K-shell fluorer technique  
from ultra-intense ( $3 \times 10^{20}$  W/cm<sup>2</sup>,  $\leq 500$  J) laser-plasma interactions on the  
Petawatt laser at LLNL**

**K. Yasuike, M.H. Key, S.P. Hatchett, R.A. Snavely**

**Abstract**

Characterization of hot electron production (a conversion efficiency from laser energy into electrons) in ultra intense laser-solid target interaction, using 1.06  $\mu\text{m}$  laser light with an intensity of up to  $3 \times 10^{20}$  W cm<sup>-2</sup> and an on target laser energy of  $\leq 500$  J, has been done by observing  $K_\beta$  as well as  $K_\alpha$  emissions from a buried Mo layer in the targets, which are same structure as in the previous 100 TW experiments but done under less laser intensity and energy conditions ( $\leq 4 \times 10^{19}$  Wcm<sup>-2</sup> and  $\leq 30$  J). The conversion efficiency from the laser energy into the energy, carried by hot electrons, has been estimated to be  $\sim 50$  %, which are little bit higher than the previous less laser energy ( $\sim 20$  J) experiments, yet the x-ray emission spectra from the target has change drastically, i.e., gamma flash.

**Contents list**

- 1 Introduction**
- 2 Experimental set-up**
  - 2.1 Target structure
  - 2.2 CCD x-ray spectrometer
- 3 Monte-Carlo K-shell x-ray yield modeling**
  - 3.1 Monte-Carlo simulation modeling
  - 3.2 Modeling results and behavior
- 4 Calibrating and testing the CCD x-ray spectrometer**
  - 4.1 CCD efficiency and eV/counts value calibration
  - 4.2 CCD energy resolution
- 5 Experimental results**
  - 5.1 Raw spectrum from the CCD
  - 5.2 Fluorescence background x-ray (photon pumped)
- 6 Processing and analysis**
  - 6.1 Simulations of K-shell line binning process
  - 6.2 Results of K-shell line binning process simulations
  - 6.3 K-shell photons production efficiency, 0.5 ps experiments
  - 6.4 Longer pulse experimental  $K_\alpha$  production efficiency results, 5 ps and 20 ps
- 7 Discussion**
  - 7.1 Electron conversion efficiencies
  - 7.2 Low electron temperature components in the hot electron spectra
  - 7.3 Background lines and determining line relations in the CCD spectrum
  - 7.4 Ratio of  $K_\alpha$  and  $\beta$  lines
  - 7.5 Ion contribution to the Mo K-shell emission
- 8 Conclusion**
- 9 References**

## 1. Introduction

In experimental study, characterization of hot electron production at the target-laser interaction region under high intensity and high laser energy is relevant to fast igniter scheme for ICF and crucial to understand other high intensity physics as well as for designing the full-scale fast igniter in NIF. The fast ignition (FI) scheme, originated by M. Tabak [1] and recently discovered very efficient ion acceleration phenomena at LLNL on Petawatt experiments, one of which potential application is a fast igniter adapting those ions [2] to make a hot spark, all depends on hot electron generation at the laser-target interaction region [3-6]. Accurate characterization of hot electron production is indispensable to estimate a needed laser energy for both types of FI to design full scale NIF fast igniter configuration, since an efficiency of hot spark generation by both the FI schemes is a function of the conversion efficiency of hot electron production, as well as to understand the physics around the high intensity laser interactions. There must be optimal laser intensity to generate optimal hot electron energy for the applications, e.g., fast igniter, which will be different for electron fast igniter and ion fast igniter and to maximize hot electron or ion number within the useful energy window in whole spectrum (fig. 1,) which determines the acceptance (emittance requirements.) This paper describes the results from the experiments with laser energy of 400 J up to 700 J, or on-target-energy of 280-500 J, and an on-target laser intensity of up to  $3 \times 10^{20} \text{ W cm}^{-2}$ , which intended to test higher laser energy and intensity condition than the previous experiment series [7-9] done on the 100 TW laser system, which will be refereed as “the previous 100 TW experiments” in this paper, done under the laser intensity of  $\leq 4 \times 10^{19} \text{ Wcm}^{-2}$  and the

laser energy of  $\leq 30$  J [7]. Larger amount of x-ray noises, e.g., gamma flash, was observed in these recent high laser-energy experiments. An optimization process for FI application may also need to consider this change, since it could dissipate an input laser energy into useless spectrum (of x-ray, thus of electron.) Investigation of effects of the laser intensity and energy on hot electron production, as well as following interesting related topics, is getting more important: 1) Directionality (angular distribution) of the hot electrons to form a spark for FI applications under a full scale FI configuration; 2) Spectrum or representative temperature(s), which might be a function of direction (angle); 3) Representative conversion efficiency from laser energy into hot electrons escaped to outside the target; 4) Time evolution of electron production, because timeframe required for FI is comparable to the disassembling time of the hot spot, which is order of 10 ps. The experiments cover the topic #3 above and some portion of the topic #2.

## **2. Experimental arrangement / Set-up**

Figure 2 shows experimental set-up. An ultra-intense laser light focused by a parabolic mirror irradiates a target. X-rays produced by energetic electrons produced at the laser-plasma interaction region are observed by an x-ray spectrometer located in backside (opposite to the laser irradiation side) of the target with an observation angle of  $30^\circ$  normal to the target. The parameter of the laser is an intensity of up to  $3 \times 10^{20}$  Wcm<sup>-2</sup>, a laser energy of 400 to 700 J, and a pulse duration of 500 fs, which is fixed for all these experimental condition. The incident laser is hit normal to the target, so there can be ignored effects of the laser polarization direction. We used a charge-

coupled device (CCD) under operated single photon mode as an x-ray spectrometer. There are significant gamma flashes from the target and the target chamber wall surrounding it, so that some filters were needed to operate in "single photon" mode. Since the CCD need to be operated under single photon mode, we choose filter thickness so that the single photon mode operation are rather assured than to obtain good pixel (photon) number of objective lines with high background x-ray level, which will be discussed in later. Reducing the photon flux other than the objective lines from the target is crucial. There are three major sources of these x-rays: 1). x-rays directly from the target, 2). bremsstrahlung x-rays produced from the electrons escaped from the target, and 3). photon pumped fluorescence x-rays. In this mode, lower energy x-rays far below the target lines at the CCD also need to be cut and it is difficult when environments has high flux of higher spectrum, which will produce fluorescence x-rays. So we located the CCD outside the target chamber to avoid these noise. The CCD was located, to reduce X-ray background noise, outside the target chamber with a distance of 4720 mm from the center of the target chamber, where a target is located. Between the target and the CCD, there is an aluminum vacuum-atmosphere septum of 0.8 mm thickness on the target chamber located about 1 m from the target. Additional aluminum filters are located between the target and the CCD. These filters are placed near the septum on the target chamber so the fluorescence x-ray from the aluminum filters have less solid angle than the material located near the CCD thus reduces fluorescence background photons from these materials. The total thickness of the filter, including the septum, was from 5.263 to

7.635 mm of aluminum. There are 7 data shots analyzed. The parameters of set-up for each data shot are shown in the "set-up" columns in the table I.

## 2.1 Target structure (chosen thickness)

In experiments, ultra-intense laser irradiates a target and generates hot electron at the laser-plasma interaction area on a front surface of the target. These electrons go through the target and emit characteristic K-shell x-rays of the target. The structure of the target is shown in the inset 1 in the fig. 2 and is same as for "the previous 100 TW experiments." The target is constitute of three layers in order to separately measure the hot electron flux at a specific depth in the solid from the effects caused by electrons generated by lasers at the laser interaction region. The front layer is intended to simulate the mass density  $\rho R$ , in (electron) FI scheme that the electrons, generated by an ultra-intense laser, need to penetrate before reaching to the location to be heated. We used to be able to estimate the hot electron temperature from the stopping power differences by changing the front layer thickness, which method will work mainly in lower electron energy region (low laser intensity, the electron energy  $E$  has been proved to be expressed as  $E \propto I^{-0.3-0.5}$  empirically up to  $10^{19} \text{ Wcm}^{-2}$  intensity [10, 11], however in these laser intensity regions, it turned out that it does not work very well as before. The front layer was made from Aluminum and chosen to be thickness of from  $0.05$  up to  $0.22 \text{ g cm}^{-2}$ , that are same as "the previous 100 TW experiments" to compare and chosen to be relevant mass density ( $\rho R$ ) to be penetrated for fast igniter scheme, which is  $\rho R$  of  $0.5 \text{ cm}^{-2}$  into heat a compressed fuel core, a density of  $200\text{-}600 \text{ g/cm}^3$ , to achieve a spark temperature of above  $15 \text{ keV}$ . The buried middle

layer is a tracer layer, which emits characteristic K-shell x-rays excited by hot electrons generated at the front surface through the front layer. These K-shell x-rays are observed by a spectrometer, so we can resolve the excitation information in a specific depth in the target material, where the tracer layer exists. We choose molybdenum for the tracer layer because Mo has high K-shell line energies, around 17.4 and 19.6 keV, respectively, for  $K_{\alpha}$ s with an intensity assignment ratio of 65.1 photon emissions out of 100 K-shell vacancies and  $K_{\beta}$ s with 11.8 emissions out of 100 vacancies [12, 13], so the photon pumping by lower energy (environmental background) photons can be avoided. The tracer layer is chosen to be 50  $\mu\text{m}$  thickness of Molybdenum. The last layer, or backside layer is made from CH of 1000  $\mu\text{m}$  thickness, which “protects from” or avoid the reflex electrons from the target once escaped to outside the target sprung back to the tracer layer by a target potential charging up. The thickness of the tracer and the protective layers are fixed for all these data shots same as for “the previous 100 TW experimental conditions.” The cut-off energy of this protective layer is 570 keV for double pass (electrons which have gone through the tracer layer and the protective layer and come back to the target, shown as (3) in the inset figure 2 of the fig. 2) and 350 keV for a single pass electron ((4) in the inset.) The relevant line energies and assignment fractions, can be observed by our spectrometer, are tabulated in the table II.

## 2.2 CCD x-ray spectrometer

We used a cooled charge-coupled device (CCD) camera, XTEA/CCD-1024 from Scientific Imaging Technologies (SITE)/Tektronix as an x-ray spectrometer, in



which each pixel in the CCD chip accepts one photon or nothing, that operation mode called “single photon mode.” The CCD is placed in a small housing, pumped down to vacuum to cool down the CCD chip avoiding a moisture condensation on it, which has a polycarbonate window with a thickness of 6 mm as an X-ray entrance. The attenuation by the window for Mo K-shell lines (17-20 keV) is negligible. There are additional filters made from aluminum to control total flux on to the CCD. The CCD camera uses SITe SI-003A scientific-grade CCD chip [14], which has 1024 by 1024 (1 mega) pixels (active area for each pixel of  $24 \times 24 \mu\text{m}^2$  each) and a depletion layer thickness of  $7 \mu\text{m}$ . A temperature of the CCD chip was maintained to be  $-24^\circ\text{C}$  to  $-30^\circ\text{C}$ . The camera was used with a controller ST-138S from Princeton Instruments and the system has a dynamic range of 16 bit, which determines energy resolution and is sufficient for these experiments. Actual energy resolution is mainly determined by property of CCD substrate of Si, so we cannot utilize whole the 16 bit dynamic range to improve the energy resolution. Total pixel number in the CCD mainly determines the accuracy of the data, a dynamic range of each line.

### **3 Monte-Carlo estimation for K-shell x-ray production in the target (universal curve)**

There are two important parameters to be interested: 1) absolute production efficiency, in photons  $\text{str}^{-1} \text{J}^{-1}$ , from electron energy into K-shell photon emissions, and 2) conversion efficiency, in %, from laser energy into hot electrons. From the experiments, we can determine production efficiencies from laser energy into K-shell emission in photons  $\text{str}^{-1} \text{J}^{-1}$ . The purpose of Monte-Carlo simulation is to obtain

absolute production efficiency, or the 100 % conversion efficiency; thus we can infer laser to hot electron coupling or conversion efficiency, which are very important for fast igniter conceptual design. The goal of the simulation/estimation is to obtain the “universal curves,” K-shell x-ray production efficiencies, or 100 % conversion efficiency from laser energy into hot electrons, from a unit laser energy input as a function of temperature (not an electron energy) for each distributions. The temperature or hot electron energy distributions in real laser conditions are needed to be measured experimentally.

K-shell photon production efficiency, from the tracer layer in the target, by assuming electron flux, generated at the front surface (laser-plasma interaction region) and go through the target, is needed to evaluate the actual conversion efficiency for real experiments from unit laser energy into hot electrons. Generally, using thicker front layer cut lower energetic electrons and gives less background x-ray noise environments, but does not have sensitivity for the electrons below its cut-off energy. If there are high energy hot electron components far above the cut-off range, distorted temperature distributions from a conventional temperature distribution like Boltzmann or Maxwellian, the K-shell emission measurement method with varying the front layer thickness does not have a sensitivity to estimate temperature very accurately, even there isn't hot-tail above few MeV. However convergence efficiency can be still inferred from K-shell emission measurements.

### **3.1 Monte-Carlo simulation modeling**

We assumed same target structure and its dimensions used in the experiments (described in the sec. 2.1) for the Monte-Carlo simulation modeling. We first obtained conversion efficiency from an electron assumed to have monochromatic kinetic energy into K-shell x-rays as a function of monochromatic electron energy by a electron-photon interaction Monte-Carlo simulation code, named Integrated Tiger Code (ITS code) [15]. The code does not have effects of electric current conveyed by collective motion of charged particles. However it still gives good estimation and reasonable agreements with experimental results for the previous experimental series [9].

It is rather more convenient and straightforward to a representative temperature, to delegate the hot electrons, assuming an energy distribution than using (monochromatic) energy to compare the conversion efficiency with real laser experiments. We choose several shapes of energy distributions of hot electrons to see effects of the distribution shape differences, i.e., Boltzmann:  $f(E) = e^{-E/T} / T$ , Maxwellian:  $f(E) = 2 E^{1/2} e^{-E/T} / \pi^{1/2} T^{3/2}$ , and relativistic Maxwellian:  $f(E) = E^2 e^{-E/T} / 2T^3$ , where  $E$ ,  $T$ ,  $f(E)$  is, respectively, electron energy, representative temperature of the distributions and number distribution of electron as a function of  $E$ . An absolute conversion efficiency as a function of representative temperature from unit hot electron energy into K-shell photons are thus obtained by integrating the distribution that is plugging in the electron-K-shell conversion efficiencies from the ITS code to the energy distribution for the temperature.

### 3.2 Modeling results and behavior

Figure 3 is the universal curves for the experimental layer structure set for targets (front Al layer: 200, 400 and 800  $\mu\text{m}$ ; tracer Mo layer: 50  $\mu\text{m}$  fixed thickness; protective CH layer: 1000  $\mu\text{m}$  fixed thickness) for the three temperature distributions, a Boltzmann, a Maxwellian, and a Relativistic Maxwellian. In lower energy region ( $\leq 500$  keV,) relativistic Maxwellian conditions give highest  $K_{\alpha}$  production among these distributions, since higher portion of the spectrum only contribute to the productions; however, in higher region, not very high energy parts do, and the Boltzmanns contain more lower energy parts than the others. Unit energy carried by electrons is distributed by an assumed distribution, so the total number of the electrons in each distribution,  $\int f(E) dE$ , is different. It is obvious from the “universal curve” that in higher electron energy, K-shell production efficiency is not very sensitive to hot electron temperature or shape of temperature distribution, however we can still estimate a conversion efficiency from K-shell photon yield, though it is hard to say about temperature (electron spectrum.) This is also plausible from the cut-off energies for electron of front layer thickness, 195, 300 and 470 keV for 200, 400 and 800  $\mu\text{m}$  Al layer, respectively. That is the case in these high laser intensity experiments both empirically and theoretically, as main lobe of the hot electron energy spectrum could be considered to be in same order of ponderomotive potential [16] theoretically determined by laser intensity,  $U_{\text{pond}} \cong \{ \sqrt{(1 + I \lambda^2 / 2.8)} - 1 \} \times 511$  [keV], where  $I$  and  $\lambda$  are on target laser intensity in  $10^{18} \text{ W cm}^{-2}$  and wavelength of laser in  $\mu\text{m}$  respectively, which comes to be  $\leq 5.9$  MeV in our experimental condition, or empirical expression  $E \propto I^{-0.3}$ , where  $E$  is electron energy, which has been proved to varied up to  $4 \times 10^{19} \text{ Wcm}^{-2}$  ( $E \leq 760$  keV) and will be 1.4 MeV if it can be assumed to be still varied for

these intensity, however we should be careful that it has not been proven for the intensity level of these experimental region. Emission in Mo  $K_\beta$  lines at the tracer layer are assumed to be proportional given in the tables II to the  $K_\alpha$  emission and estimated 100 % conversion efficiency  $K_\alpha$  and  $K_\beta$  production

#### **4. Calibrating and testing the CCD x-ray spectrometer**

The CCD is calibrated for actual eV/counts value for relevant x-ray lines and the efficiency for these lines (sec. 4.1). The energy resolution of the CCD is experimentally tested, which will be used to a starting point of binning processing for experimental results (sec. 4.2). We tested the configuration described in the sec. 2 on actual Petawatt experimental conditions and found that a relatively strong signal with a line location of ~25 keV based on actual CCD calibration data In order to confirm the origin of this line, we tested the CCD on linac, which is described in sec. 4.3.

##### **4.1 CCD efficiency and eV/counts value calibration**

For specific CCD, we need to obtain eV/count value, and acquisition efficiencies of the CCD for relevant lines. For hard x-rays, a CCD will register different eV/count value to use as a spectrometer from the eV/count value for low energy photons, e.g., visibles and UVs, which determined by the work function of Si (substrate material of the sensor) and a Fano factor [17], since Compton effect will be dominant in absorption process in high energy region. We used  $^{109}\text{Cd}$  radioactive source for CCD calibration, which emits  $^{109\text{m}}\text{Ag}$  22 keV  $\gamma$ -rays. The source requires longer time of 300 s to accumulate to obtain enough events, which is considerably

longer than the accumulation period for actual data shots, thus register wider width of the peaks. In experiments, we used 10 ms of accumulation time for the CCD, which is sufficiently longer than the laser-interaction time-scale. An eV/count value and a CCD photon acquisition efficiency for the 109mAg 22 keV line were first obtained, and then the efficiencies for relevant objective lines are derived by using the photoionization cross-section values [18-20] of Si. The eV/count value was determined to be 22.2 eV/count. The CCD efficiencies for Mo  $K_{\alpha}$  and  $\beta$  were, respectively, 9.37 % and 6.54 % out of the photons hit CCD. The efficiencies for relevant lines in these experiments and the photoionization cross-sections for them are shown in the table II.

#### 4.2 CCD energy resolution

In actual experiments, an energy resolution is determined by both the eV/count value and effects of dark (background) subtraction. Typical background level of the CCD was 400 up to 900, depending on the CCD temperature and condition of the CCD controller. That dark level is same level of the counts corresponding to the signals by photons of relevant lines, so dark subtraction is necessary for data analysis. Subtracting the darks improves the energy resolution of the spectrometer and allows using smaller bin width for the data processing, which will be described later. In experiments, dark images were taken before and after each data shot with same CCD (temperature condition), and the dark were subtracted from the data images before any data analysis. In order to determine the effects of dark subtraction against the energy resolution, we tested to take dark images (null) without incident lasers to evaluate the reminders after dark subtraction. Examples of the histograms of these

dark subtracted null images are shown in fig. 4a. Each set of histogram bars in the figure shows different image accumulation time of the CCD. The shapes of histograms of the images are very close to Gaussian distributions and depend on accumulation time and the temperatures of the CCD. Using fig. 4a, we determined full width at the half maximum (FWHM) by fitting the data by a Gaussian (smooth curves in the figure), and plotted the FWHM as a function of accumulation time, shown in the fig. 4b. The actual resolution of the CCD can be considered to be the eV/count value times the FWHM. The FWHM is less than 9 counts for an accumulation time of less than one second. If the CCD is operated under single photon mode, we can expect that the resolution will be equal to the FWHM obtained from the null shot without incident laser light. Using least needed tight bin width is desirable in data processing, since the signals obtained by the CCD are in low level. A binning process in obtained histogram was necessary to get better (processed) signal-to-noise ratio. Each line width within the K-shell groups ( $\alpha$  or  $\beta$ ) is far narrower than the resolution of  $\sim 200$  eV and the binning width should be greater than the resolution width and greater than the width of the line groups. Operating temperature change of the CCD changes absolute level of noise floor, but the gain (eV/counts value) remains constants. Locations of the signal peaks slightly walk by fluctuation of the temperature. Which is clearly seen on the curve, a 300 s accumulated condition since the accumulation time is long and within that time the temperature slightly fluctuate though the chip temperature is being maintained by the controller and is within set temperature range (less than  $0.5^\circ\text{C}$ ) all the time.

## 1 Experimental Results

### 5.1 Raw spectrum from the CCD

Figures a to e in the fig. 6 show raw results, after dark subtraction, from the experiments. The curves in blue in the figures show spectra, or histogram with a bin width of 1, and the curves in red are pixel usages, or integral of histogram, as a function of energy, or counts. In order to make sure that all the CCD operations were under single photon mode, we checked pixel usage for each shot. It is found that total environmental photon number other than objective lines from the targets are higher than expectation estimated from “the previous 100 TW experiments” conditions and its  $K\alpha$  photon production efficiencies, and also found that there is relatively strong Sn and Pb lines excited by (environmental) gamma flash, in which the Sn  $K_{\alpha 2}$  and 1 lines (25.19 keV) are strongest (fig. 6, and in sec. 5.2). As seen in every figures in the fig. 5, the shape of spectra has very different from the spectra on lower laser energy shots [7, 21, 22], and have very significant large slope due to the gamma flash and bremsstrahlung x-rays, even though these experiments used thicker filters, that modified the spectra at the CCD from those at the target. Figure 6 is a horizontally magnified spectrum of fig. 6f. The lowest curve in grey in the figure is the raw spectrum or a histogram with bin width of 1. Signals in bottom in red show expected Mo  $K_{\alpha}$ , and  $K_{\beta}$  lines. The Mo  $K_{\alpha}$ , and  $K_{\beta}$  line groups are, respectively, located around 800, 900. The other curves above the raw spectrum in the figure are examples of binning process, with several bin width and starting locations, whose details are described in sec. 6.



## 5.2 Fluorescence background x-ray (photon pumped)

There are several sources of x-rays, contribute to the background noise of the CCD: 1). Bremsstrahlung from escaped hot electron from the target hit at the target chamber wall and around the CCD; 2). Gamma pumped fluorescence from target chamber. From the other experiments on the Petawatt laser, about 1 % of total energetic electrons produced in a target was determined to escape from it reach beyond the inner target wall, thus produce bremsstrahlung x-rays. As will be described in the discussion section, the tin and lead inside the CCD camera will be excited by severe gamma flash in these experiments, and have been actually observing these lines even though there are no such external materials located near the targets and the CCD, and the cross-sections of photon pumped K-shell excitation are low.

In order to confirm the origin of the line that is not from the Mo  $K_{\alpha}$ s offset by uniform background (relatively large number of background photons hit into each CCD pixel) to be appeared as the 25 keV line, we had the same CCD camera tested under a 5 MeV linac x-ray environments, used as a "Petawatt background x-ray simulator," and reproduced the signal located at the same energy even though there is no Mo target. Figure 5 shows the spectra (histograms) of the linac test (fig. 5f) and those of "real" data shots (fig. 5a-e). The hard x-ray spectrum on Petawatt experiments is determined by measurements using radiochromic films and thermoluminescence dosimeter (TLD) [5]. The photon numbers from the line amplitude are well agreeable with an estimation, assuming an amount of Sn contained in solder on the circuit board in the CCD camera housing and the solid angle of the tin to the CCD,

determined by spatial relationship. These lines cannot be seen by a regular efficiency calibration procedure (using  $^{109}\text{Cd}$  source) since the radio active source is not enough strong to photon-pump these lines to appear. It is clearly shown that the observation system for these experiments should be tested carefully under high x-ray fluency environments to avoid "line contamination." The spatial relationship between the tin around the CCD and the CCD chip is fixed in the CCD housing, and is not affected by experimental set-up. Which means, in other words, acquiring efficiency of these photons emitted within the housing is constant over the experiments though the excitation flux (gammas produced at the target) of these tin  $K_\alpha$  is changed by the filter (bremstrahlung from the chamber wall might be not affected by the filter thickness if the other condition remain same,) in contrast to the Mo lines from a target, whose attenuation is changed by the filter thickness though the (electron) excitation of Mo is not affected by the filter thickness change. The observation of the  $K_\alpha$  lines from tin around the CCD and of the Mo K-shell lines from the target could be complementary. Using a Sn filter is not advisable since we can use this tin excitation as a monitor (though the current status is crude) of the environments so that the gamma flash level is consistent over the experimental series.

## 6 Processing and analysis

In real experiments, background components in the spectrum from the CCD have fast changing (high frequency) components which look random with a standard deviation of amplitude of  $\sim 9$  around the Mo  $K_\alpha$  and  $K_\beta$  lines, and slow changing big slope base line (slope) components. Expected signal levels, derived from the filter

conditions in the table I and the K-shell photon production based on the “universal curves” in the Fig. 3, are small, we had evaluated binning process on simulated signals, which consist of signals of several photon level and backgrounds, to know behaviors of analysis process to obtain photon numbers for  $K\alpha$  and  $K\beta$  photons of Mo.

### 6.1 K-shell line binning process simulation

In order to evaluate the binning or “skimming” process of Mo K-shell photons, signal from the CCD contains K-shell photons and background noises, are assumed and tested effects of changing the bin width and starting point for each bin, or center of each bin, since their responses for low photon level were not obvious. The assumed signals consist of uniform constant offset of 150 counts, a white Gaussian noise with  $\sigma = 9$  counts, which is about in same level in the experimental results around the lines of the signals, and K-shell photons. The conditions having K-shell photons of 10, 20, 40, 60 and 90 for each  $K_\alpha$  and  $K_\beta$  line groups has been tested. Total number of  $K_\alpha$  photons and  $K_\beta$  photons are to be set equal and line intensity ratio within each  $K_\alpha$  and  $K_\beta$  lines group are proportional to the tabulated line ratio in table II. This assumption is reasonable since we need to use considerable thick filter for the CCD in actual experiments so at the CCD,  $K_\alpha$  and  $K_\beta$  photon number are modify to be almost identical. Estimated  $K\alpha / K\beta$  ratio for “real” filter conditions are shown in the table I. The fig. 7 shows examples of effects of starting points for each bin with a bin width of 13, which are relevant to actual data processing condition. Each curve shows different bin starting location, or center of the bin condition, and in some bin starting condition, the signals cannot be seen, though all the bin width were the same. We can

expect that if we choose suitable bin width, we can raise the signal clearly even though photon number of signal is considerably low.

However, calculated areas of the peak area, defined as  $S1$  in the fig. 9, in binned curves typically register higher number than the supposed signal. This is occurred mainly due to the peak broadening by binning and the base width of the peak is enlarged several times in the same order of bin width, which are wider than objective line group width. In order to correctly estimate the peak area, we calculated base line, and the area, defined as  $S3$  in the fig. 8, above the base line is calculated.

These areas,  $S1$  and  $S3$ , depends on starting bin location even though the bin width is same. In order to avoid subjective results affected by selection of a starting bin location, due to a selection of starting bin location, we calculated areas for each binned curve having different starting bin location, and then averaged these areas over all the starting bin locations. This averaging process eliminates an effect of start bin location, and gives a unique value, which independent of a starting bin location. In this paper, we call the averages of  $S1$  and  $S3$  as  $\overline{S1}$  and  $\overline{S3}$ , respectively. We confirmed that the value of averaged  $S1$  and  $S3$  will converge to the  $\overline{S1}$  and  $\overline{S3}$  in large signal region, but for a small signal condition,  $S1$  does not register right value, or registers “constant floor.” The standard deviation ( $\sigma$ ) of the  $S3$ s could be used to evaluate the “convergeness.”

The eV/count number is consistent among the different shots and the locations of the line don't change very much. We chosen a location and a width to calculate the number of K-shell photons within it as that the width is narrower than the peak seen

on the binned graph but enough wider to contain all the lines of groups and location to be set to the center of the peak.

## 6.2 Results of K-shell line binning process simulation

Figure 9 shows the response of the binning process as a function of bin width for the cases, input photon numbers of a). 10 pixels, b). 20, c). 40, and d). 90. In Fig. 9d, an  $\overline{S1}$  and an  $\overline{S3}$  for a same assumed signal level of 90 pixels are shown as an example.  $\overline{S1}$  registers much higher photons# than  $\overline{S3}$  or assumed level, however, the ratio of the difference between  $\overline{S1}$  and  $\overline{S3}$  to the signal level will decrease for large photon# case, and will converge to a same number. In the fig. 9,  $K\beta$  signal can be seen smaller bin width than  $K\alpha$  because  $K\beta3$  and 1 contain 85 % of the total  $K\beta$  intensity and are located very closely together within less than one count.  $K\alpha$  signal intensities is more evenly distributed, e.g., 34.4 and 65.6 % for  $K\alpha2$  and  $K\alpha1$  lines, respectively, so the  $K\alpha$  signal processing needs larger bin width of 4.7 counts than for  $K\beta$  to contain  $K\alpha2$  and  $K\alpha$ . We found that for weak  $K\beta$  signal, restricting the band width (bin width,) which gave up  $K\beta2$  and 4 which contain 11.86 and 2.56 % of total  $K\beta$  intensity, is more favorable to reduce noise than to cover whole the  $K\beta$  line

A response function of the binning process, e.g., photon number given by the binning process, or output photon numbers versus input or assumed photon, is obtained by plotting the  $\overline{S3}$  at the specific bin width as a function of input signal. Figure 10 shows the response function of  $\overline{S3}$  for a bin width of 11, which is relevant to actual data processing. In low signal level, there is “floor” seen in the figure. K-

shell intensity ratios for relevant lines are shown in the K-shell intensity ratio column in the table I.

### 6.3 K-shell photons production efficiency

Figure 11 shows  $K\alpha$  and  $K\beta$  photon production efficiency from unit laser energy into  $K\alpha$  and  $K\beta$  photons, plotted as a function of the front layer thickness, in top axis, or front layer surface density  $\rho$ , in the bottom axis. In data analysis for “real” experimental condition, we used 31-points binomial smoothing function [23] and a simple 21-points moving average after it. The points in blue in the figure represent  $K\alpha$  production efficiencies, use the left axis, and the points in red correspond to  $K\beta$  production, on the right axis. The right axis in the figure is scaled 0.18123,  $K\beta / K\alpha$  intensity ratio, of the left axis, so that the reading at the left axis for the  $K\beta$  points directly gives  $K\alpha$  equivalent numbers for the  $K\beta$  plots. Some of  $K\alpha$  data processing did not give meaningful results because  $K\alpha$  signal is less prone to be affected by noise though the photon numbers of  $K\alpha$  and  $K\beta$  are in a same level, as predicted in section 5. There are good agreements between these  $K\alpha$  and  $K\beta$  results. The  $K\alpha$  production efficiency for these experiments are determined to be  $0.7\text{-}2.5 \times 10^9$   $K\alpha/\text{str}$  per unit laser energy. The error bars are obtained from the standard deviations ( $1\sigma$ ) of the S3s. The blue, green and red curves in the fig. 11 are, respectively, 100 % laser-electron conversion efficiencies for a temperature of 2 MeV with Boltzmann, Maxwellian, and relativistic Maxwellian distributions, quoted from the universal curves. With comparing these 100 % figures and actual K-shell production coefficients, we can

obtain electron production (or acceleration) efficiencies, or conversion efficiencies from lasers into electrons. Details of the convergence efficiency estimation will be discussed in the sec. 7.1.

#### **6.4 Results from 5 ps and 20 ps longer pulse Petawatt experiments**

We had measured Ka production efficiencies using same target structure for 5 ps and 20 ps pulse width. In those experiments, laser energies were about the same level as recent 0.5 ps shots, however the intensities on the targets were different. The intensity and power level for 5 ps shots were determined to be  $1.0 \pm 0.2 \times 10^{19} \text{ W cm}^{-2}$  and  $\sim 60 \text{ TW}$ , and  $2 \pm 0.4 \times 10^{18} \text{ W cm}^{-2}$  and  $\sim 20 \text{ TW}$  for 20 ps shots, respectively. In those experiments, noise level to the CCD spectrometer was much less, and the spectrometer was not suffered bad signal to noise ratio or small photon number in the object lines. The backgrounds were also much less level than these 0.5 ps shorter pulse experiments. Typical  $K\alpha$  photon number was from  $10^4$  to 700. The raw data from 5 ps and 20 ps shots and fitted curves using the universal curves to estimate a temperature and a conversion efficiency, are shown in the fig. 12 and 13, respectively. Solid curves in the figures shows chi-square fitting results assuming a Boltzmann, Maxwellian and relativistic Maxwellian temperature distributions, with using weighting, which are determined as an inverse of the error bar width between the top and bottom of the error bar for each points. As seen in the plots of raw data and the fitting results for these data, long pulse experimental results show the fitting has good sensitivity for estimating the temperature as well as conversion efficiencies. The temperatures and conversion efficiencies for Boltzmann, Maxwellian, and relativistic

Maxwellian for 5 ps data sets are, 818 keV and 19.4 %, 620 keV and 20.3 %, and 353 keV and 17.1 %, respectively, and 328 keV and 13.9 %, 269 keV 12.9 %, and 174 keV 11.7 % for 20 ps data set. The curves for the three temperature distributions are almost identical with almost same conversion efficiencies though the representative temperatures differ. Resultant temperatures, conversion efficiencies for the distributions are tabulated in the table III.

## **7. Discussion**

### **7.1 Electron conversion efficiencies from lasers into the energy carried by hot electrons**

From these K-shell production efficiency, efficiency of electron acceleration can be precisely estimated if we know the temperature of hot electrons and the shape of energy spectrum of the hot electrons. Though we have not understood an exact shape of energy spectrum of hot electron generated at the laser-plasma interaction area on the target, the temperature could be roughly estimated from the empirical relation (sec. 3.2.) Using this estimated temperatures of between 1 MeV and 4 MeV, and assuming the fact that the universal curves do not register much deviations among the distributions for this region, we can still expect that the conversion efficiency can be estimated without much difference even though we do not know precisely about the electron energy distribution shape or its temperature. We chosen a temperature of 2 MeV and a shape of the distribution Maxwellian as a “standard” case, since the Maxwellian’s curves are located between Boltzmann’s and Relativistic Maxwellian’s distributions. Conversion efficiencies are calculated for  $K_{\alpha}$  and  $K_{\beta}$  results for each



data shots. The K-shell production efficiencies determined experimentally and the standard conversion efficiencies are shown in the table IV. Figure 14 are plots of the standard conversion efficiencies obtained from these experiments as well as from the previous experimental series. For these Petawatt series, plus and minus error bars are, respectively, obtained from Relativistic Maxwellian and Boltzmann condition, because Boltzmann gives higher values for 100 % K-shell photon production efficiencies than others, and relativistic Maxwellian gives lowest among them in these region, so the efficiency can be bracketed between these values. The electron production efficiencies are determined to be  $47.4 \pm 18.1$  % ( $1\sigma$ ),  $42.3 \pm 15.7$  % and  $65.2 \pm 25.6$  % for 2 MeV Boltzmann, Maxwellian, and Relativistic Maxwellian distributions, respectively. We also calculated conversion efficiencies for temperatures of 1 and 4 MeV with Boltzmann, Maxwellian and Relativistic Maxwellian distributions, and then we obtained average efficiencies and standard deviations ( $\sigma$ ) using  $K_\alpha$  and  $K_\beta$  efficiencies together for each case. These average and  $\sigma$  values for those cases are tabulated in the table V.

If we assume that a each point in a same data set has uniform error bars, and a chi-square fit with a uniform weighing value (of unity) for every points, would be used to estimate the uniform error bar, which is square root of a value, which are resultant chi-square from the fit divided by number of data set. We performed this uniform weighting fit to obtain uniform errors for each data set. The fine dash curves in the figures represent the results from uniform weighting fits, and as seen in the figures, the curves are not very different from the fit results using weighting, and resultant uniform error bars are very consistent with the error bars experimentally

obtained. This uniform weighting fitting process could be used to estimate error bars using smaller data set. The other curves show fit with assuming different predetermined Maxwellian temperature to estimate conversion efficiency for that temperature. Resultant uniform errors are tabulated in the table V.

Summary over these and previous experimental series for the laser-electron conversion efficiencies, and other relevant parameters, e.g., relative intensities and temperatures, including the previous series are compiled in the table VI, and plotted in the fig. 15. The temperature scaling relation as a function of laser intensity is roughly determined to be  $\propto I^{0.4}$  from the graph. These experiments are done under an intensity of one order higher and a temperature of 2 to 3 times higher than the experiments done ever.

## **7.2 Low electron temperature components in spectra**

If the spectrum is assumed to be multi temperature, the energy of lower components are above the cut off of the 200 or 400  $\mu\text{m}$  Al font layers, because there is no significant difference between the different thickness. Thus we can conclude that there is no significantly large low temperature components in the hot electron spectra.

## **7.3 Background lines and determining line relations in CCD spectrum – references in the background to determine absolute line relations**

There are significant amount of tin and lead inside the CCD camera as a form of solder, which have very large solid angle against the CCD than that of the target. The tracer K-shell lines should not be close to the lines from these environmental material elements, e.g., Pb  $L_{\beta 2}$  and 1 (in stronger order, 12.6 keV,) Pb  $L_{\beta 5}$  (13.015

keV,) Pb L<sub>γ</sub>1 (14.765 keV,) Sn K<sub>α</sub>2 and 1 (25.19 keV,) Sn K<sub>β</sub>3 and 1 (28.47 keV) and Sn K<sub>β</sub>2 and 4 (29.12 keV.) The energies of the object lines should be enough high to have sufficient x-ray acquisition efficiency for the CCD (Si,) since its efficiency decreases as well as the resolution deteriorates because the Compton process dominates for higher photon energy. Using Mo as the tracer conforms to these requirements. These environmental lines are useful to determine the absolute location in the spectrum since dark image, background taken before a data shot, is subtracted from the data shot so the peak may shift if there is temperature drift between the image acquisitions, and in these experimental condition, tracer signals are weak so using the environmental “pilot” lines, which are more strong than the tracer lines, are more accurate to determine actual line relations or an offset level of the count value.

#### **7.4 Using both K<sub>α</sub> and K<sub>β</sub> enlarge working dynamic range (photon#) (ratio of K<sub>α</sub> and β lines)**

Using K<sub>β</sub> signals is useful in noisy environment, which dominated by both low energy x-rays and gamma flashes, which potentially pump higher x-ray lines. We experienced higher noise level than the previous “100 TW experiments.”

Thicker filters estimated from the previous experimental conditions were required to reduce photon flux on the CCD chip to operate the CCD under single photon mode. The thicker filters modifies the intensities of the K<sub>α</sub> and β lines severely, and the ratio of K<sub>β</sub> to K<sub>α</sub> is getting close to unity from 0.18123 as shown in the set-up column of table I, since the transmission for K<sub>β</sub> is greater; thus using only K<sub>α</sub> is no longer advantageous. This effect is seen in the results column of the same table that some of

the  $K_\alpha$  failed to obtain results, though  $K_\beta$  counterparts for the same shots were successfully obtained. The previous 100 TW laser experiments were done using much thinner filters, so the  $K_\beta/K_\alpha$  ratio is much closer to the original ratio of 0.18123. Summary of the filter conditions over these and the previous experimental set-up are compiled in the table VII.

### 7.5 Ion contribution to the Mo K-shell emission

Effects of K-shell x-rays excited by energetic ions inside the target has been estimated. The motivation is ion acceleration by induced potential by conductivity gaps between layers in the target. The flux of electron is estimated to be more than  $10^{14}$  electrons per incident laser shot from other experimental result [5]. Assuming that the electrons go through within the laser pulse duration of 0.5 ps, a current of 32 MA is inferred. If the resistance is 10 m $\Omega$ , an acceleration voltage of up to 320 kV (depending on the initial location of the particle to be accelerated) will appear at the transition of the layers. The production efficiency of K-shell x-rays are 0.3 to 80 barns for 1 to 3 MeV/a.m.u or  $3.8 \times 10^{-6}$  to  $4.41 \times 10^{-4}$   $K_\alpha$  photons/p [24]. Which is lower than that for the hot electrons, 0.73 to 84 barns or  $1.3 \times 10^{-3}$  to  $2 \times 10^{-3}$   $K_\alpha$ s a proton for the same energy range, and x-rays from ions could not be dominant in these experiments, however higher current experiment will be needed to consider this point. The ion particle energy (MeV/nucleon) or at least energy spectrum range could be estimated from the K-shell line shifts,  $\sim 100$  eV for 10-40 MeV range, however, the shifts as a function of incident particle energy is not measurable in the current spectrometer resolution.

The ratio  $K\alpha / K\beta$  will change as a function of incident particle energy, e.g., Mo  $K\alpha / K\beta = 0.192 \pm 0.002$  to  $0.198 \pm 0.003$  for 2.88 MeV/a.m.u. to 12.5 MeV/a.m.u. [25], Cu  $K\alpha / K\beta = 7.0$  to  $5.2$  for 10 to 40 MeV oxygen (O) ions or  $0.625$  to  $2.5$  MeV/a.m.u. [26]. The ions inside the target could be below that energy range and also due to thick filter and the not sufficient dynamic range for the lines (number of pixels within the CCD) of the spectrometer, the ratio measurements of  $K\alpha / K\beta$  for ion energy is not applicable for these experiments. If the dynamic range for  $K\beta / K\alpha$  ratio measurements were greatly improved, we could estimate particle energies from variation of the ratio.

## 8 Conclusion

### 8.1 Conversion efficiencies from lasers into electrons

K-shell photon production efficiency per unit laser energy per solid angle are obtained by utilizing  $K_\alpha$  and  $K_\beta$  emission from buried Mo layer in the target, and are determined to be a  $K_\alpha$  yield of from  $7 \times 10^8$  to  $2.5 \times 10^9$   $K_\alpha \text{ str}^{-1} \text{ J}^{-1}$  ( $K_\beta$  numbers are converted to equivalent  $K_\alpha$  numbers). Electron production efficiencies or acceleration efficiencies are obtained assuming energy distributions of hot electrons and their temperatures. The production efficiencies are between 35 to 66 %, and mostly around 50 %, which are higher than previous experiments done under less on target laser intensity and energy level condition. In the previous papers, it was concluded that the hot electron temperature does not change very much even laser intensity or laser energy changed and said that a representative hot electron temperature which independent from laser condition can be assumed, and there is some new high

intensity mechanism which limit the average energy of electrons above  $10^{18} \text{ W cm}^{-2}$ . However it is most likely due to the effects that the K-shell emission with changing front layer thickness does not have enough sensitivity for high electron energy region that far surpasses the stopping range of the front layer for electrons, seen very clearly in the universal curve. The conversion efficiency does not change very much in this region as a function of electron temperature though, a measurements of electron spectrum apart from the target [28], which registered very high energy components up to 55 MeV. Hard x-ray measurements using radiochromic film shows that there were 40 to 50 % of laser energy were converted into hot electrons and more than 2.9 %, or 11 J, of input energy was converted into very hard x-rays of harder than 0.5 MeV in forward hemisphere (backside the target) [29]. Those conversion efficiency results from the other methods are consistent with the results from K-shell measurements.

## 8.2 Future experimental proposal

In higher laser energy experiments in the future (from a point of view of the investigation rather for the high intensity physics than optimizing the irradiation parameter for FI application,) x-ray environments, which have higher fraction of high energy components, e.g., gamma flashes which already suffers our experiments, are expected to be worse and will have to choose experimental geometry and filter material conditions to control total x-ray flux to, or signal to noise (s/n) ratio on the CCD. One of the solution will be using x-ray baffles between the target and the CCD, or using composite filer material, e.g., Be and Al stacked layers. In higher laser intensity experiments, there will be higher electron temperature, so we can expect the

ambiguities of electron conversion efficiency due to uncertain electron energy spectrum shape or temperature themselves.

From recent experiments [5], we have observed proton emissions, which seems to be sufficiently energetic for FI, however we have not confirmed that the ion flux are scalable as a function of laser spot size (with same on target laser intensity level) and is need to be clarified. In these "high flux condition," controlling to get more favorable s/n configuration would be crucial.

## 9. References

1. M. Tabak, J. Hammer, M.E. Glinsky, W.L. Kruer, S.C. Wilks, J. Woodworth, E.M. Campbell, and M.D. Perry, "Ignition and high gain ultrapowerful lasers," *Phys. Plasmas* **1** p.1626 (1994.)
2. M. Roth, T.E. Cowan, M.H. Key, S.P. Hatchett, C. Brown, D.M. Pennington, M.D. Perry, R.A. Snavely, S.C. Wilks, and K. Yasuike, "Fast ignition by intense laser-accelerated proton beams," *Phys. Lett.*, to be submitted.
3. M.H. Key, "Progress in Fast Ignitor Research with Nova Petawatt Laser Facility," UCRL-JI-132178 Lawrence Livermore National Laboratory (November 1998.)
4. S.P. Hatchett, C.G. Brown, T.E. Cowan, E.A. Henry, J. Johnson, M.H. Key, J.A. Koch, A.B. Langdon, B.F. Lasinski, R.W. Lee, A.J. Mackinnon, D.M. Pennington, M.D. Perry, T.W. Phillips, M. Roth, T.C. Sangster, M.S. Singh, R.A. Snavely, M.A. Stoyer, S.C. Wilks, and K. Yasuike, "Electron, photon, and ion beams from the relativistic interaction of Petawatt laser pulse with solid targets," *Phys. Plasmas*, printing.
5. R.A. Snavely, M.H. Key, S.P. Hatchett, T.E. Cowan, M. Roth, T.E. Phillips, M.A. Stoyer, E.A. Henry, T.C. Sangster, M.S. Singh, S.C. Wilks, A. MacKinnon, A.Offenberger, D.M. Pennington, K. Yasuike, A.B. Langdon, B.F. Lasinski, J. Johnson, M.D. Perry, and E.M. Campbell, "Intense High Energy Proton Beams from Petawatt Laser Irradiation of Solids," *Phys. Rev. Lett.*, to be printed (2000.)
6. A.P. Fewes, P.A. Norreys, F.N. Beg, A.R. Bell, A.E. Dangor, C.N. Danson, P. Lee, and S.J. Rose, "Plasma Ion Emission from High Intensity Picosecond Laser Pluse Interactions with Solid Targets," *Phys. Rev. Lett.* **73**, 1801 (1994.)
7. K.B. Wharton, Thesis, sec. 4 and 5, University of California, Los Angeles (1998.)
8. K.B. Wharton, S.P. Hatchett, S.C. Wilks, M.H. Key, J.D. Moody, V. Yanovsky, A.A. Offenberger, B.A. Hammel, M.D. Perry, and C. Joshi, *Phys. Rev. Lett.* **81** 822 (1998.)

9. M.H. Key, M.D. Cable, T.E. Cowan, K.G. Estabrook, B.A. Hammel, S.P. Hatchett, E.A. Henry, D.E. Hinkel, J.D. Kilkenny, J.A. Koch, W.L. Kruer, A.B. Langdon, B.F. Lasinski, R.W. Lee, B.J. MacGowan, A. MacKinnon, J.D. Moody, M.J. Moran, A.A. Offenberger, D.M. Pennington M.D. Perry, T.J. Phillips, T.C. Sangster, M.S. Singh, M.A. Stoyer, M. Tabak, G.L. Tietbol, M. Tsukamoto, K. Wharton, and S.C. Wilks, "Hot electron production and heating by hot electrons in fast ignitor research," *Phys. Plasmas*, **5** 1966 (1998.)
10. F.N. Beg, A.R. Bell, A.E. Dangor, C.N. Danson, A.P. Fews, M.E. Glinsky, B.A. Hammel, P. Lee, P.A. Norreys, and M. Tatarakis, "A study of picosecond laser-solid interactions up to  $10^{19}$  W cm<sup>-2</sup>," *Phys. Plasmas* **4** 447 (1997.)
11. M. Roth at GSI, private communication.
12. G. Audi, and A.H. Wapstra, "The 1995 update to the atomic mass evaluation," *Nuclear Physics A* **595** 409-480 (1995.)
13. S.Y.F. Chu, L.P. Ekstr, and R.B. Firestone, "WWW Table of Radioactive isotopes, database version 2/28/99 from URL <http://nucleardata.nuclear.lu.se/nucleardata/toi/>" (1999.)
14. SITE Lit. No. SI-003A, version date: 12/21/95, <http://www.site-inc.com/pdf/003datsh.pdf>.
15. "ITS Version 3.0: The Integrated TIGER Series of Coupled Electron/Photon Monte Carlo Transport Codes," SAND91-1634 (March 1992.)
16. Scott C. Wilks, and William L. Kruer, "Absorption of Ultrashort, Ultra-Intense Laser Light by Solids and Overdense Plasmas," *IEEE J. of Quantum Electronics* **IEJQA7 33**, 1954 (1997.); W.L. Kruer, and S.C. Wilks, "Introduction to ultra-intense laser-plasma interactions," in "Advances in Plasma Physics," AIP, New York, p. 16-25, (1994.)
17. D.H. Lumb, E.G. Chowanietz, and A. Wells, "X-ray measurements of charge diffusion effects in EEV Ltd. Charge-coupled devices." *Optical Engineering*, **26** 773 (1987.); D.H. Lumb, and A.D. Holland, "Event Recognition Techniques in CCD X-ray Detectors for Astronomy," *Nuclear Inst. and Method*.
18. D.E. Cullen, et. al, "The 1989 Livermore Evaluated Photon Data Library (EPDL)," UCRL-ID-103424, Lawrence Livermore National Laboratory (March 1990.)
19. D.E. Cullen, et. al, "Tables and Graphs of Photon-Interaction Cross Sections from 10 eV to 100 GeV Derived from the LLNL Evaluated Photon Data Library (EPDL,) Part A: Z=1 to 50, Part B: Z=51 to 100," UCRL-50400, **6** Rev. 4, Lawrence Livermore National Laboratory (October 1989.)
20. S.T. Perkins, et. al, "Tables and Graphs of Atomic Subshell and Relaxation Data Derived from the LLNL Evaluated Atomic Data Library (EADL)," UCRL-50400, **30**, Lawrence Livermore National Laboratory (October 1991.)
21. Paul Lee Choon Keat, "Picosecond laser-solid target interactions at Intensities Greater than  $10^{18}$  W cm<sup>-2</sup>," Ph. D. Thesis, Imperial College, University of London (1996.)
22. Private communications with K.A. Tanaka at ILE, Osaka University, Japan.
23. P. Marchand, and L. Marmet, *Review of Sci. Inst.* **54** 1034 (1983.)



24. Md Rashiduzzaman Khan, D. Crumpton, and P.E. Francois, "Proton induced x-ray production in titanium, nickel, copper, molybdenum and silver," J. Phys. B **9** p. 455 (1976.)
25. T.K. Li, and R.L. Watson, " $K\beta/K\alpha$  intensity ratio for x-ray production by fast deuterons,  $\alpha$  particles, and carbon ions," Phys. Rev. A **9** p. 1574 (1974.)
26. J.D. Garcia, R.J. Fortner, and T.M. Kavanagh, "Inner-Shell Vacancy Production in Ion-Atom Collisions," Rev. of Modern Phys. **45** 111 (1973.)
27. Thomas Cowan and Thomas Phillips at LLNL, private communications.
28. M.H. Key, E.M. Campbell, T.E. Cowan, S.P. Hatchett, E.A. Henry, J.A. Koch, A.B. Langdon, B.F. Lasinski, R.W. Lee, A. MacKinnon, A.A. Offenberger, D.M. Pennington, M.D. Perry, T.J. Phillips, M. Roth, T.C. Sangster, M.S. Singh, R. Snavely, M.A. Stoyer, S.C. Wilks, K. Yasuike, "Studies of the Relativistic Electron Source and Related Phenomena in Petawatt Laser Matter Interactions," (UCRL-JC-135477REV1) First Int'l Conf. On Inertial Fusion Sciences and Applications (IFSA), Bordeaux, France, Sept. 12-17, (1999.)
29. Vsevolod V. Balashov, "Interaction of Particle and Radiation with Matter" ISBN 3-540-60871-0 Springer Press, in p.78-79 Sec. 3.5 "Relativistic Effects: The Bethe-Bloch Formula," (1997.)

Set-up							Results					
Target front layer	Shot#	Distance [mm]	Filter thickness Al [mm]	Attenuation for K $\alpha$	Attenuation for K $\beta$	K $\beta$ /K $\alpha$ ratio after the filter	d $\Omega_{\text{CCD}}$ [str]	Laser energy (on target) [J]	K $\alpha$ Production Eff. [K $\alpha$ s J $^{-1}$ str $^{-1}$ ]	K $\beta$ Production Eff. [K $\beta$ s J $^{-1}$ str $^{-1}$ ]	Conversion efficiency (2 MeV maxwellian)	
											[%] K $\alpha$	[%] K $\beta$
Al 200 $\mu\text{m}$	29050407	4724.3	7.635	2.614E-05	5.621E-04	3.90	2.3E-06	316		2.88E+08		46.1
Al 400 $\mu\text{m}$	29041424	4724.3	5.262	6.947E-04	5.756E-03	1.50	2.3E-06	293		2.96E+08		52.1
	29050416	4724.3	6.120	2.122E-04	2.482E-03	2.12	2.3E-06	272	2.54E+09	2.42E+08	81.0	42.6
Al 800 $\mu\text{m}$	29042815	4724.3	6.120	2.122E-04	2.482E-03	2.12	2.3E-06	459	5.01E+08	2.45E+08	17.7	47.6
	29052013	4724.3	5.262	6.947E-04	5.756E-03	1.50	2.3E-06	287	1.60E+09	1.83E+08	56.4	35.6

Table I Set-up parameters and experimental results.

### Si Photoionization cross-section

				CCD Efficiency	
X-ray Energy [KeV]	I [%]	X-section [barn]	Rel. Eff. Ratio	[%]	
Pb L $\beta$ 2, 1	12.610	11.730	776.47	5.555	25.187
Pb L $\beta$ 5	13.015	0.411	713.83	5.107	23.155
Pb L $\gamma$ 1	14.765	1.780	479.87	3.433	15.566
Sn K $\alpha$ 2, 1	25.192	71.560	93.48	0.669	3.032
Sn K $\beta$ 3, 1	28.472	12.110	63.78	0.456	2.069
Sn K $\beta$ 2, 4	29.121	2.565	59.52	0.426	1.931
<b>Mo K<math>\alpha</math></b>	<b>17.443</b>	<b>65.100</b>	<b>288.84</b>	<b>2.066</b>	<b>9.369</b>
Mo K $\alpha$ 2	17.374	22.400	203.54	1.456	6.602
Mo K $\alpha$ 1	17.479	42.700	190.25	1.361	6.017
<b>Mo K<math>\beta</math></b>	<b>19.655</b>	<b>11.802</b>	<b>201.6</b>	<b>1.442</b>	<b>6.540</b>
Mo K $\beta$ 3, 1	19.601	10.050	203.54	1.456	6.602
Mo Kb3	19.590	3.420			
Mo K $\beta$ 1	19.607	6.630			
Mo K $\beta$ 2, 4	19.671	1.752	190.25	1.361	6.017
Mo Kb2	19.965	1.450			
Mo K $\beta$ 4	19.998	0.302			
<b><sup>109m</sup>Ag K<math>\alpha</math></b>	<b>22.103</b>		<b>139.79</b>	<b>1.000</b>	<b>4.534</b>
<sup>109m</sup> Ag K $\beta$	24.817		97.83	0.700	3.173

Table II Line assignments.

Temperature [MeV]	Boltzman		Maxwellian		Relativistic Maxwl.	
	Average [%]	$\sigma$ [%]	Average [%]	$\sigma$ [%]	Average [%]	$\sigma$ [%]
1	35.2	12.8	34.4	12.4	44.0	17.0
2	47.4	18.1	42.3	15.7	65.2	25.6
4	66.4	25.8	57.4	22.0	88.7	34.8

Table III Electron conversion efficiencies for the distributions shape and the temperatures.

Experimental series	Laser Energy [J] (on target)	Pulse width [ps]	Power [TW]	Relative Intensity	Temperature [MeV] ( $\propto I^{0.3-0.5}$ )	Relative Temperature	Conversion Eff. [%]
100 TW	30 - 12	0.4	40	1	0.3 - 0.6	1	31 (30 - 47)
	30	0.4	80	1	0.3 - 0.6	1	41 (25 - 60)
Petawatt	325 - 425	20	20	0.25	0.18 - 0.36	0.6	12 (7 - 15)
	250 - 350	5	60	1	0.3 - 0.6	1	15 - 25
	290-460	0.5	$\leq 1.4$	10	0.6 - 1.8	2 - 3	50 (35 - 65)

Table IV Summary of 100 TW and Petawatt series results.

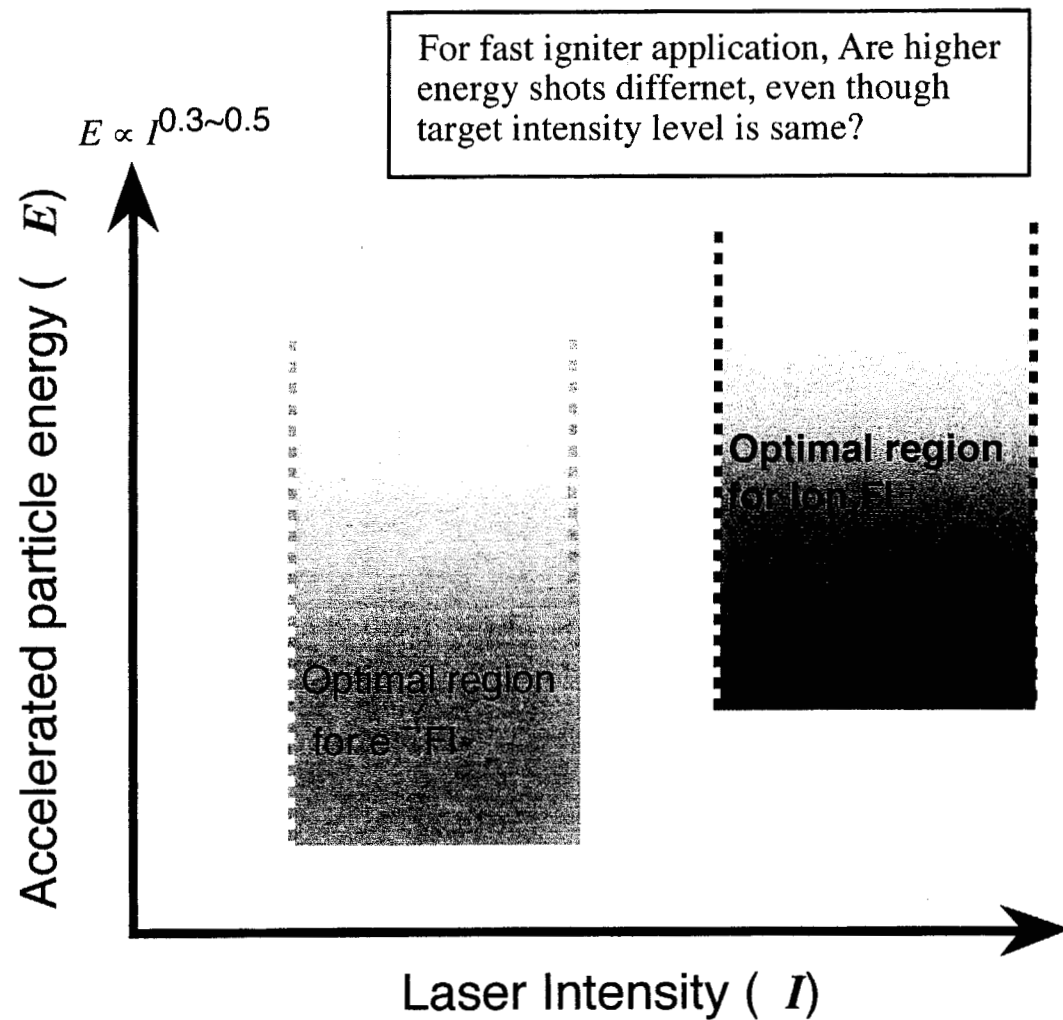
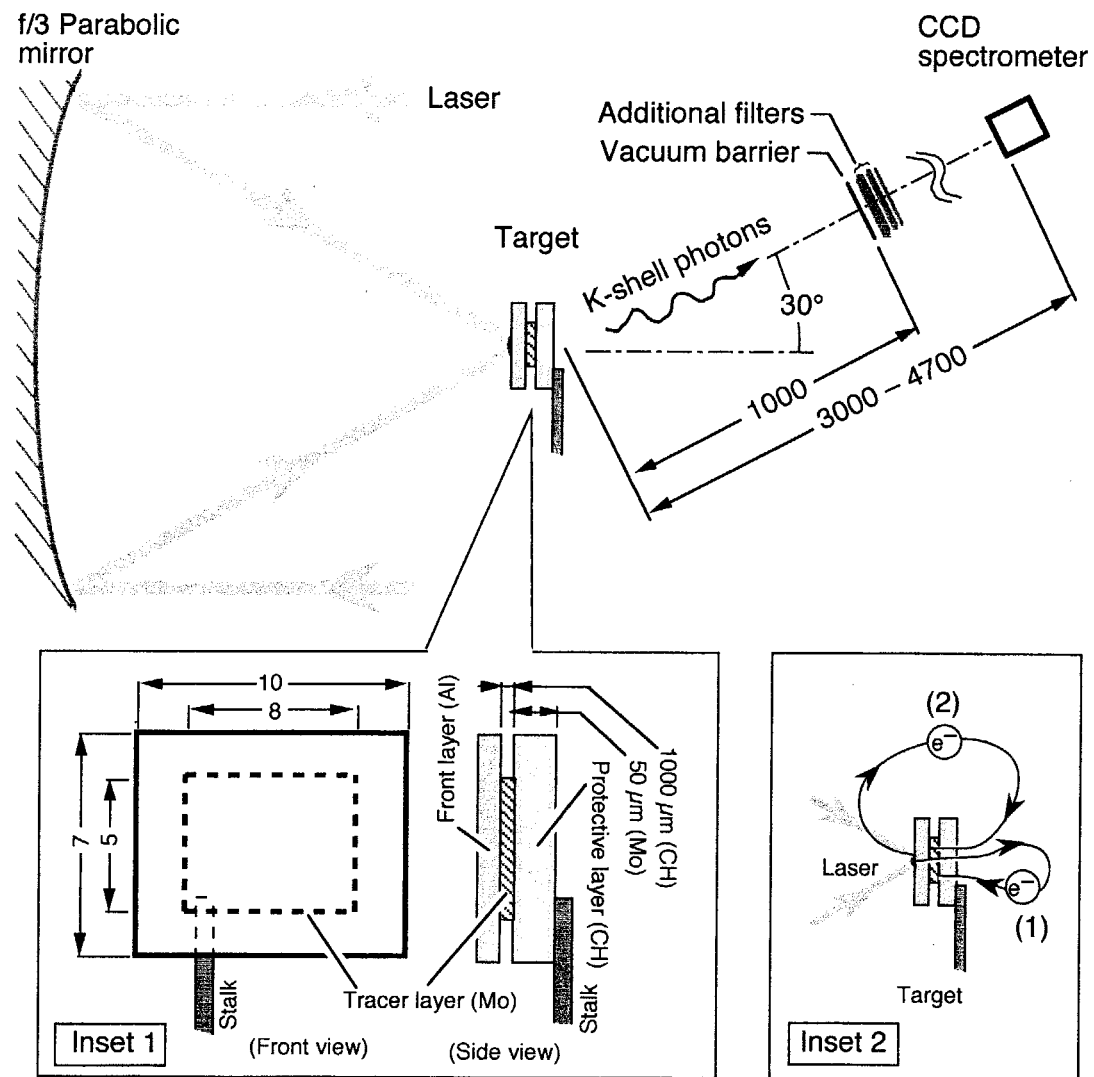


Fig. 1 Spectrum requirements for FI schemes.



Notes: Dimensions in mm otherwise noted (1 mm = 39.37 mil); Not to scale.

Fig. 2 Experimental Set-up.

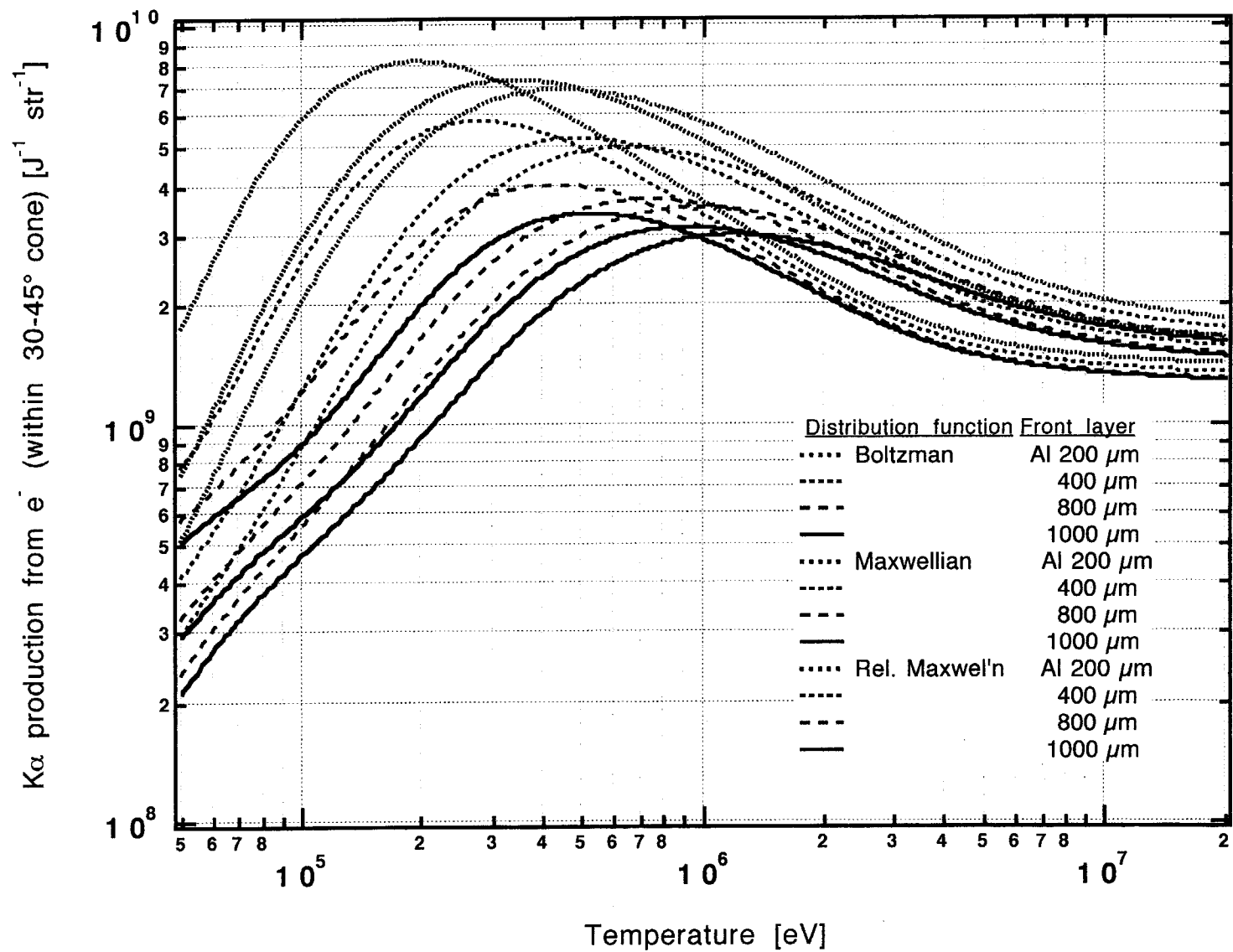
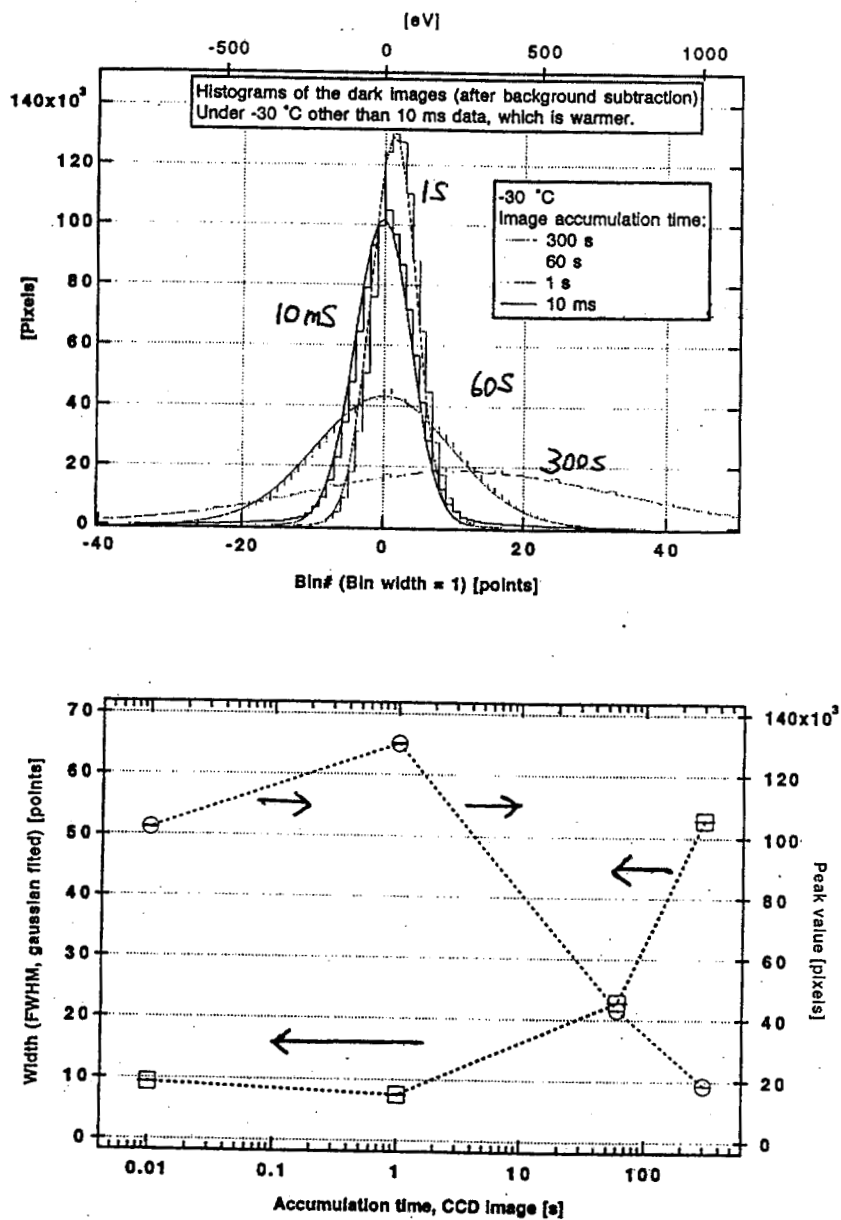


Fig. 3 Universal Curves.



Fig. 4 Dark Image Distributions



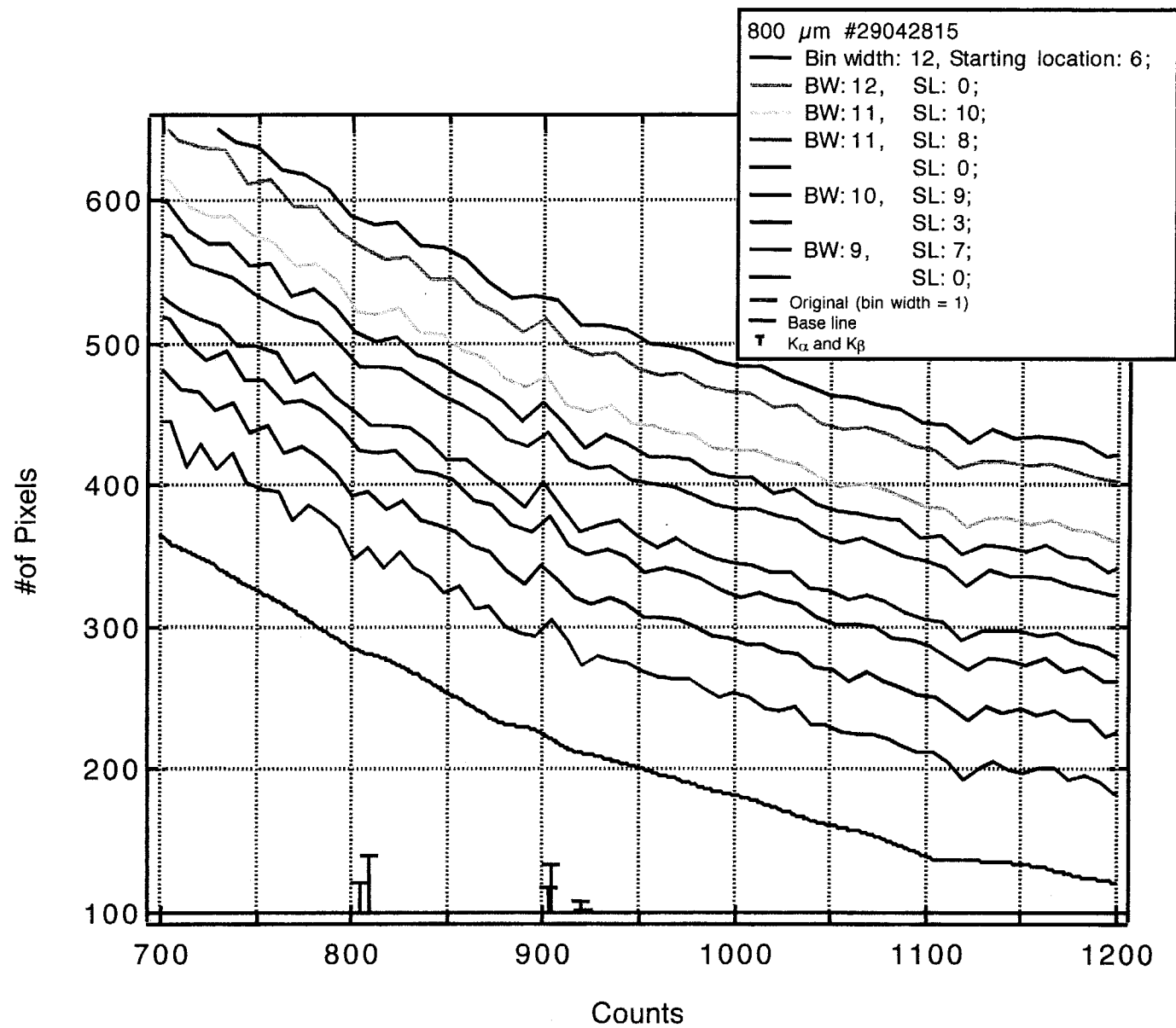


Fig. 5 Typical Petawatt Data Histograms

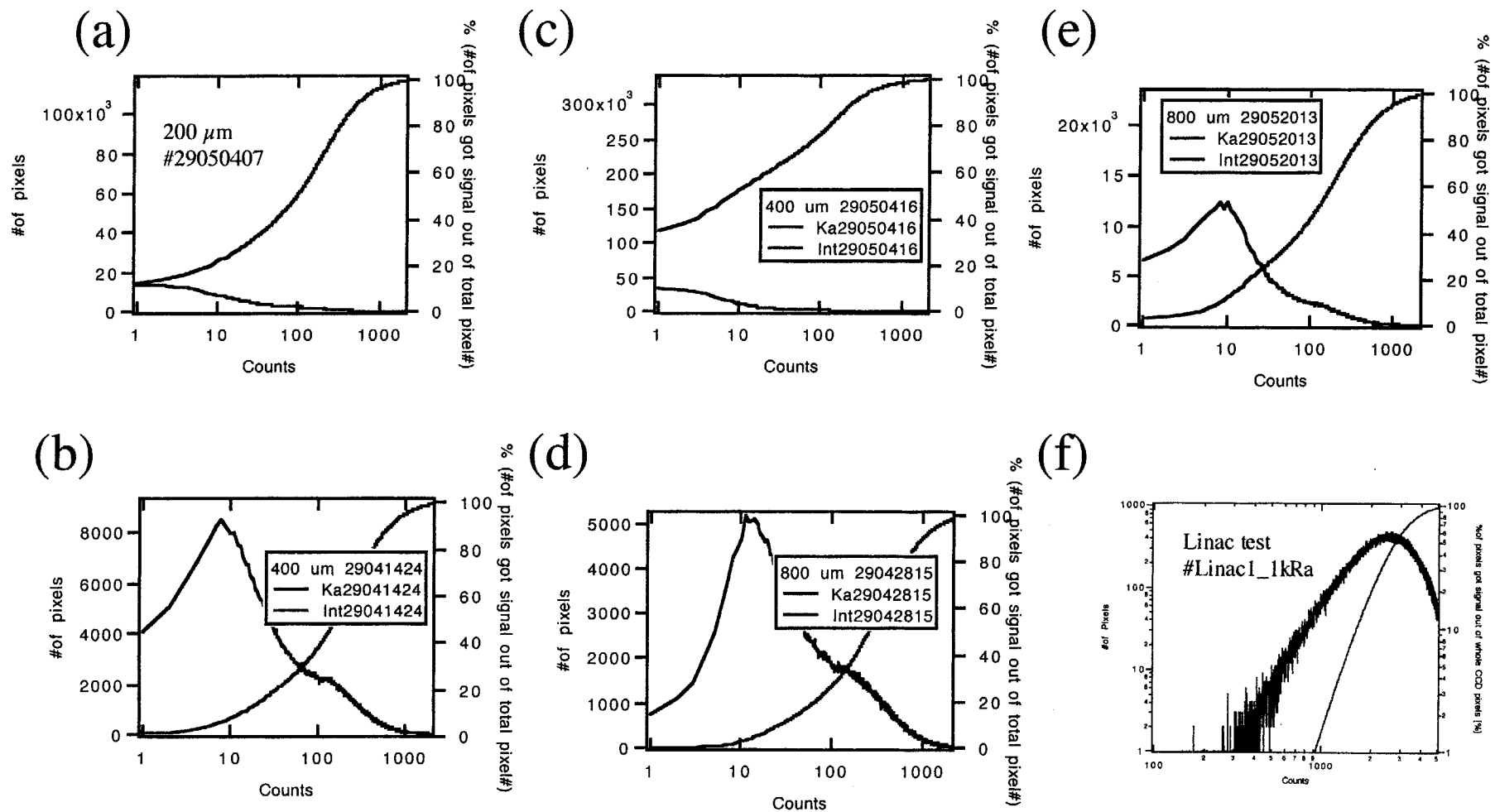


Fig. 6 Pixel usage ratio out of whole pixel  
as a function of energy.

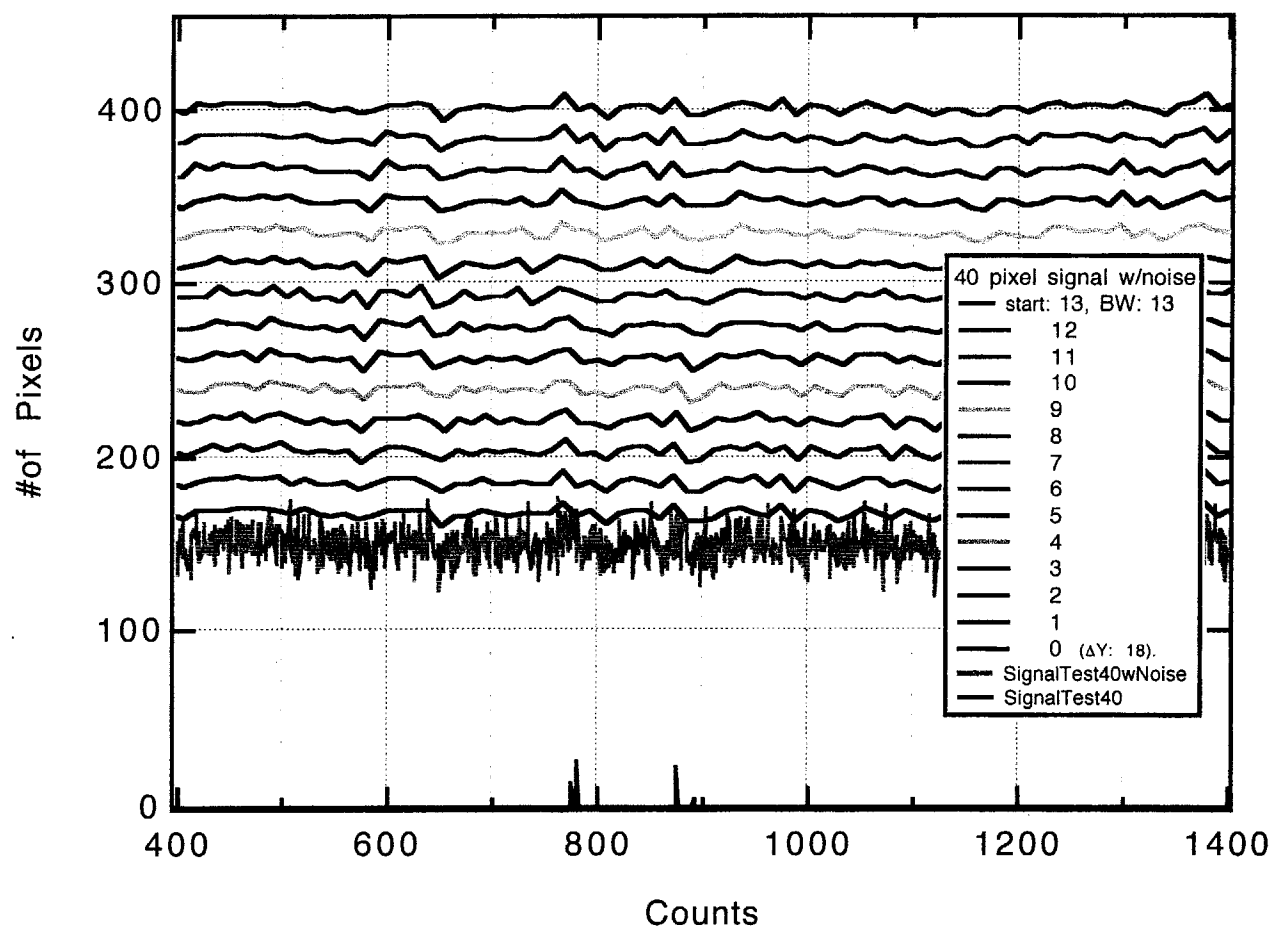


Fig. 7 An example of effects of starting bin location.

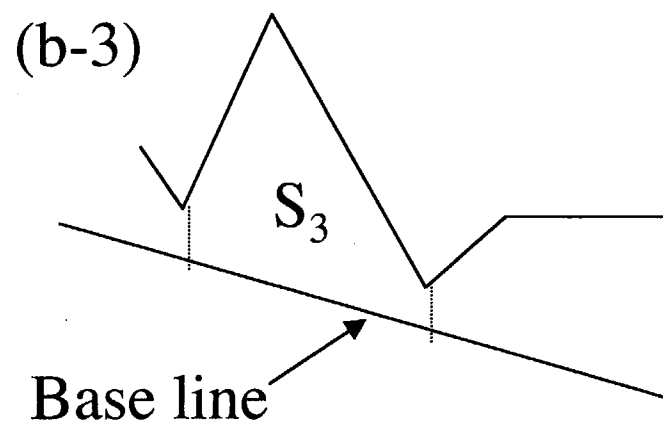
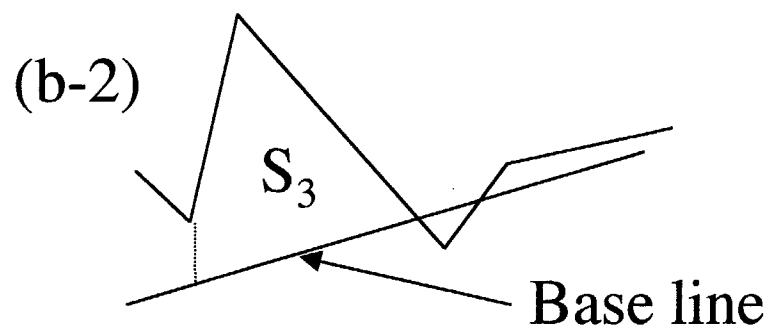
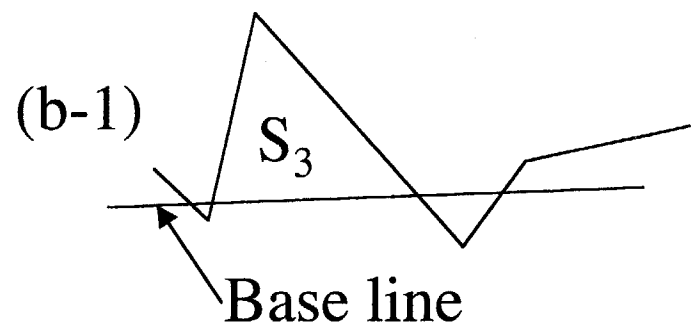
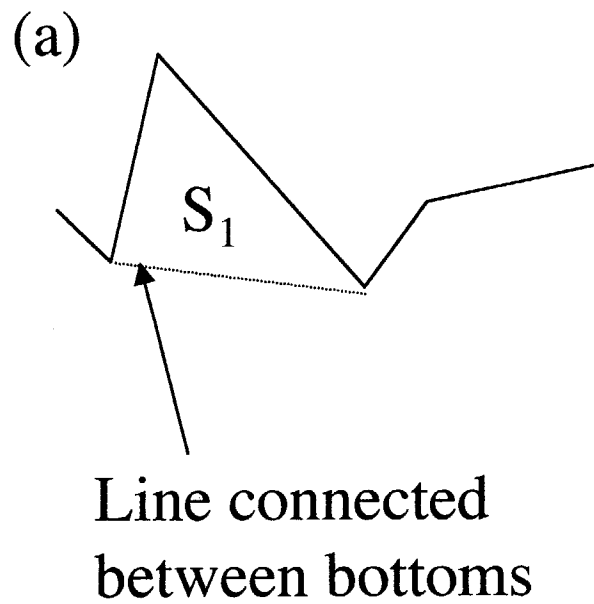


Fig. 8 Definition of  $S_1$  and  $S_3$ .

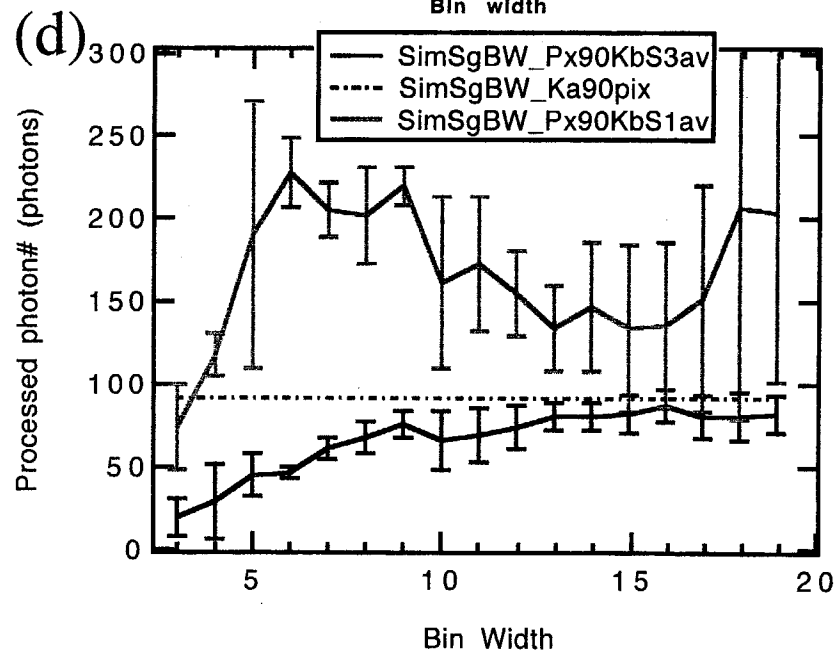
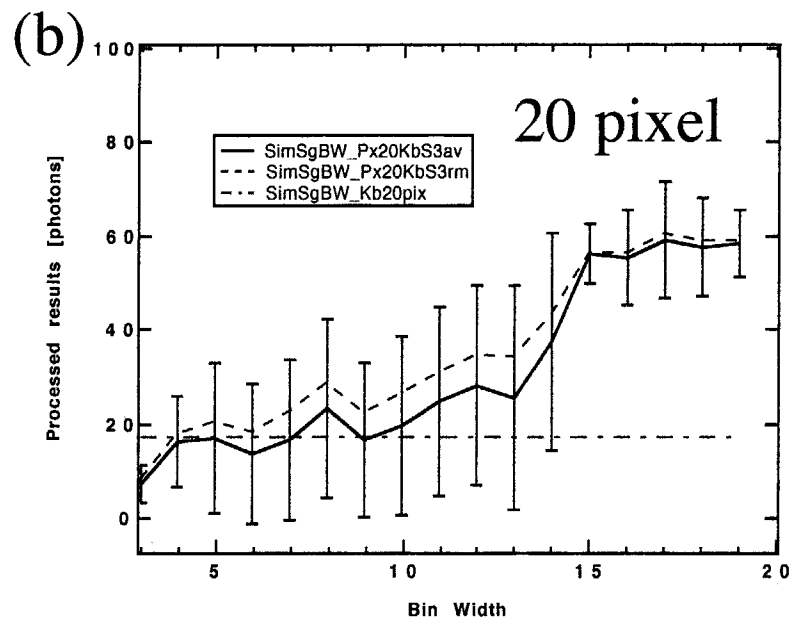
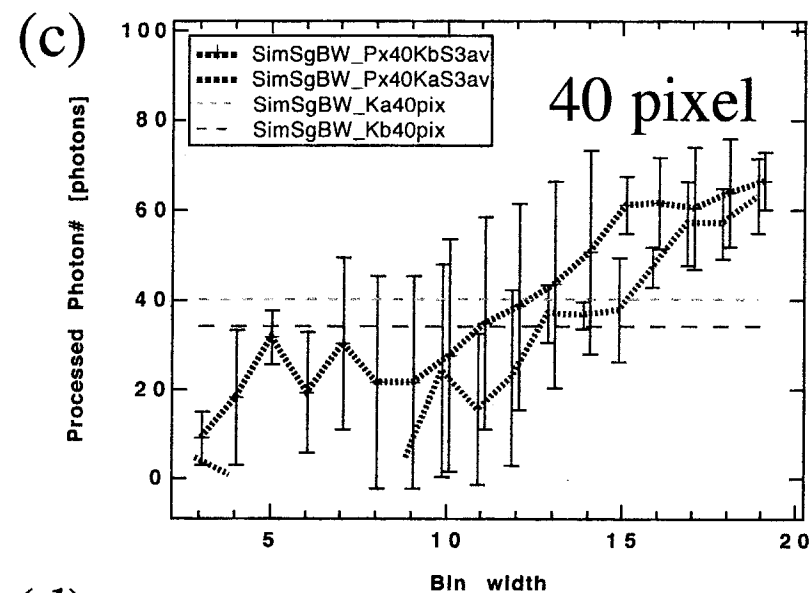
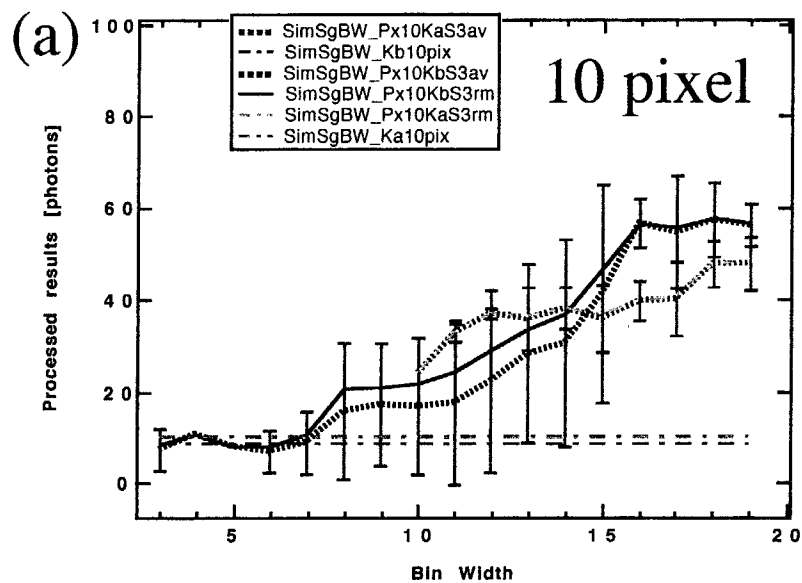


Fig. 9 Sim Signal vs. Bin width

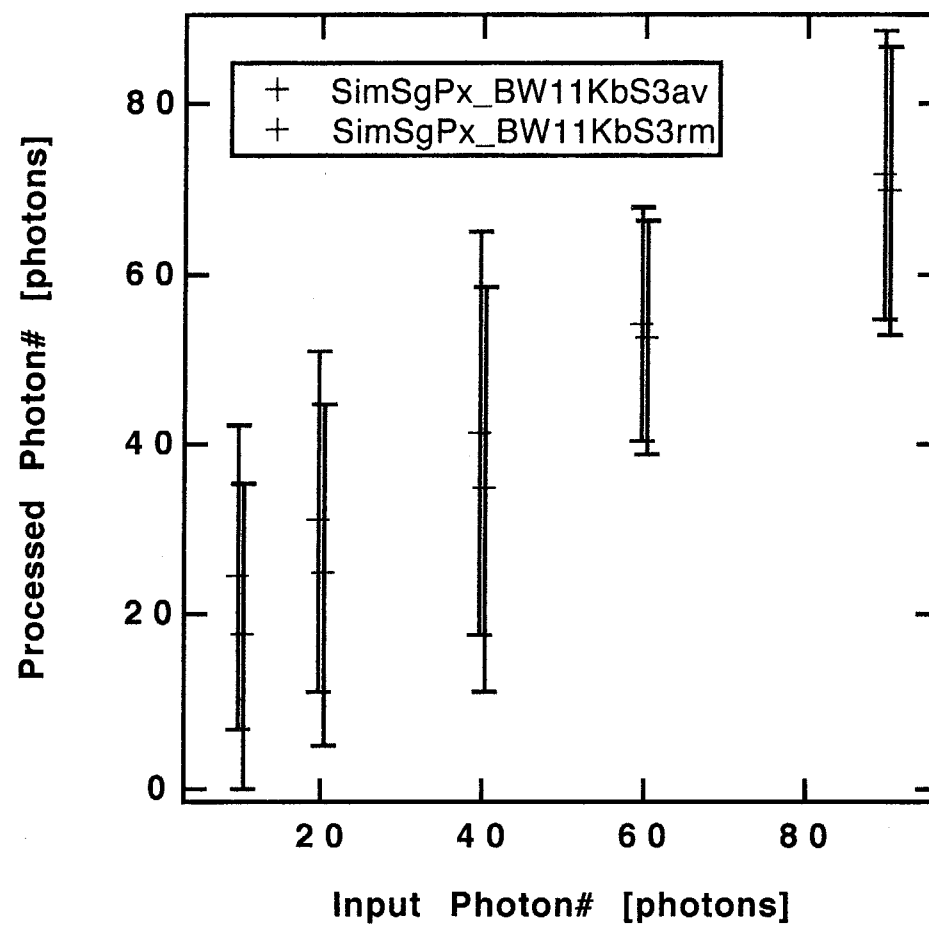


Fig. 10 Small signal response curve for a bin width of 11.

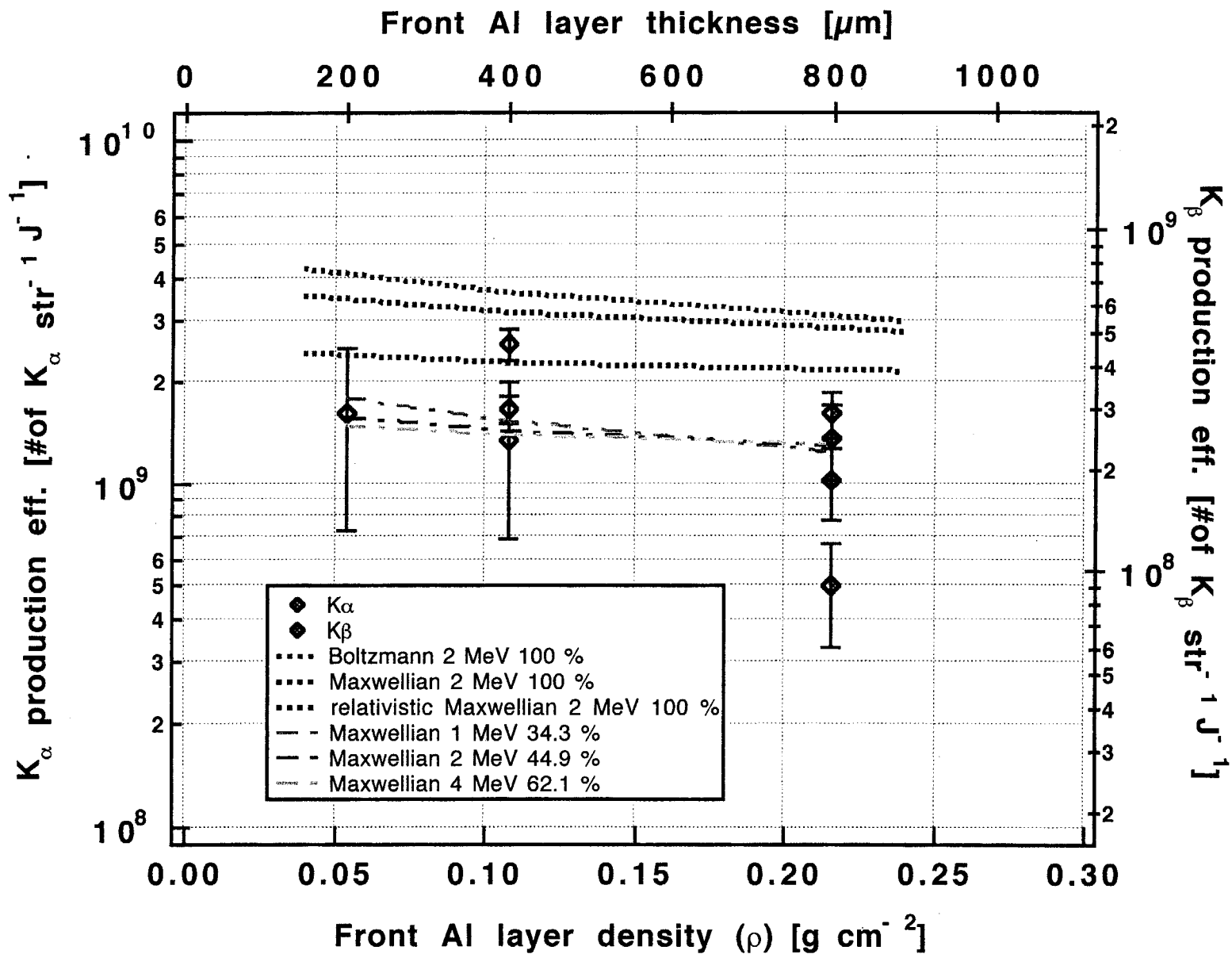


Fig. 11 The 0.5 ps experimental results.



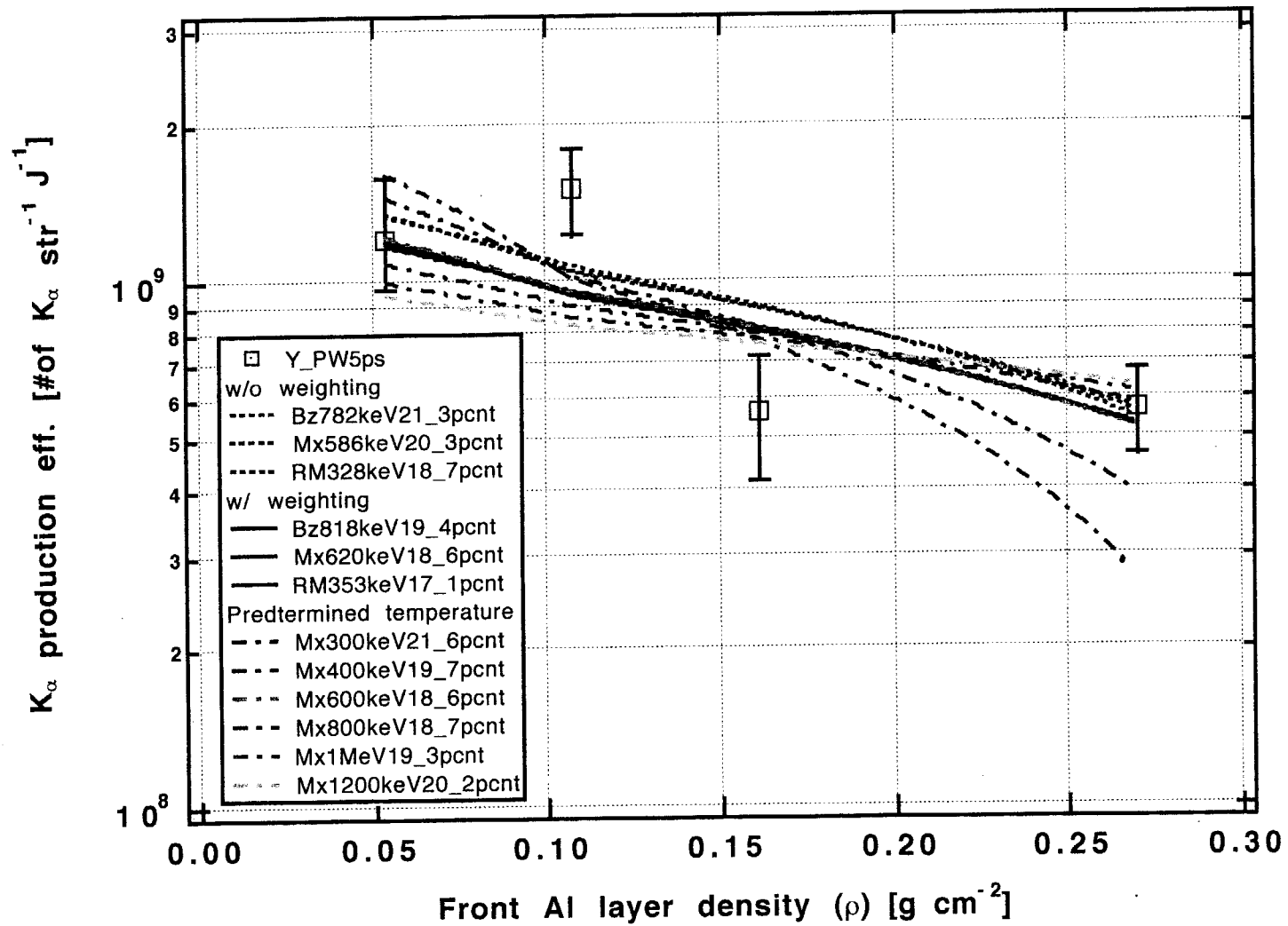


Fig. 12 The 5 ps experimental results.

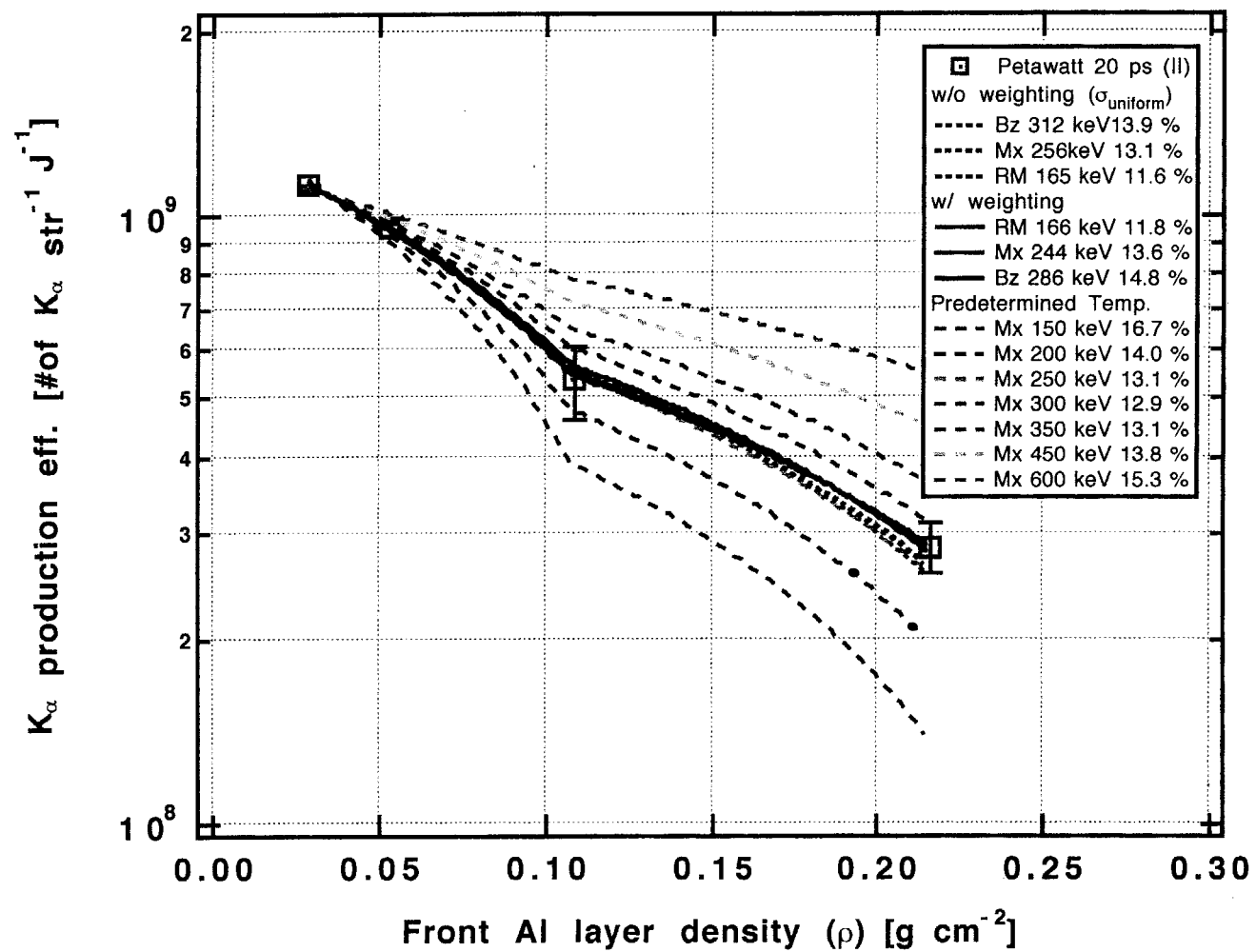


Fig. 13 The 20 ps experimental results.

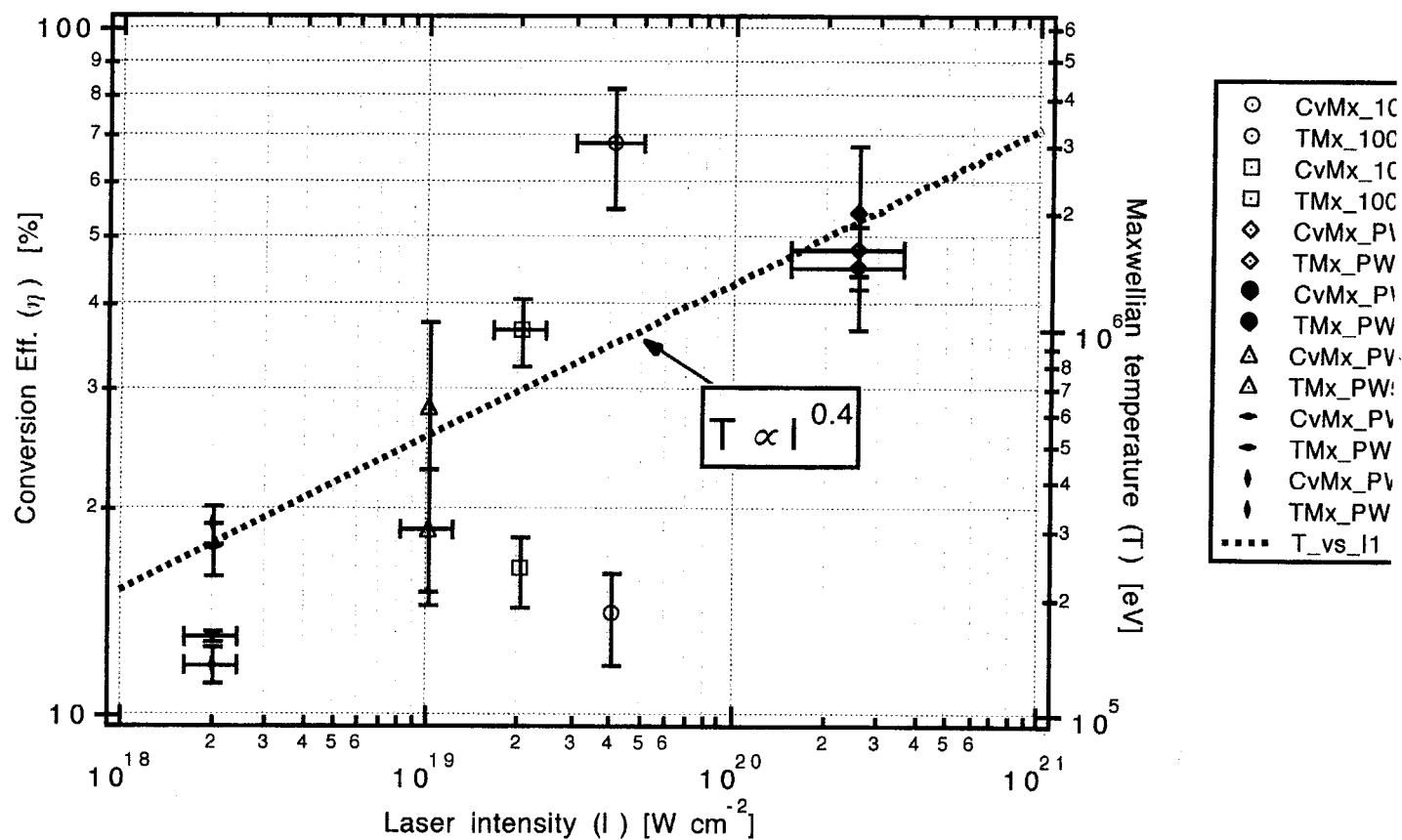


Fig. 14 Hot electron production efficiency overview.

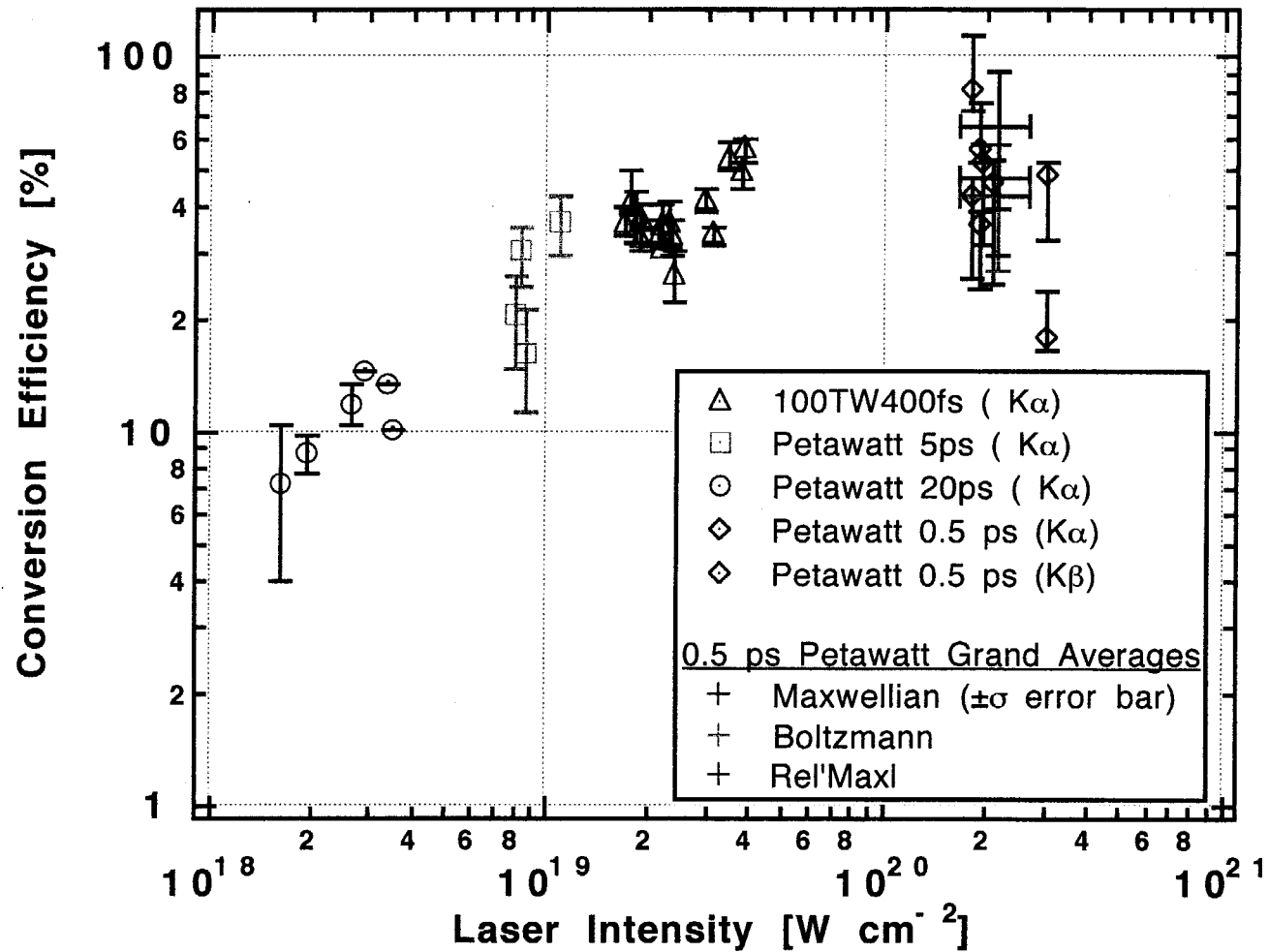


Fig. 15 Hot electron production efficiency overview.